

Nematic versus Kekulé phases in twisted bilayer graphene under hydrostatic pressure

Miguel Sánchez Sánchez¹, Israel Díaz¹, José González², and Tobias Stauber¹

¹ *Instituto de Ciencia de Materiales de Madrid, CSIC, E-28049 Madrid, Spain*

² *Instituto de Estructura de la Materia, CSIC, E-28006 Madrid, Spain*

(Dated: April 9, 2024)

We address the precise determination of the phase diagram of magic angle twisted bilayer graphene under hydrostatic pressure within a self-consistent Hartree-Fock method in real space, including all the remote bands of the system. We further present a novel algorithm that maps the full real-space density matrix to a reduced density matrix based on a $SU(4)$ symmetry of sublattice and valley degrees of freedom. We find a quantum critical point between a nematic and a Kekulé phase, and show also that our microscopic approach displays a strong particle-hole asymmetry in the weak coupling regime. We arrive then at the prediction that the superconductivity should be Ising-like in the hole-doped nematic regime, with spin-valley locking, and spin-triplet in the electron-doped regime.

Introduction. Twisted bilayer graphene (TBG) forms when two graphene layers are rotated with respect to each other with a relative twist angle θ . Under a set of commensurable angles θ_i ,¹ the system constitutes a perfect crystalline structure (*moiré lattice*) where Bloch's theorem applies. Moreover, for so-called magic angles a vanishing Fermi velocity resulting in flat bands near the charge neutrality point (CNP) has been predicted.^{2,3} The first *magic angle* is found to be $\theta \sim 1.05^\circ$.⁴

In 2018, TBG tuned around the first magic angle was shown to host insulating phases⁵ near half-filling of the hole-like moiré minibands next to a superconducting dome phases,⁶ similar to what happens in cuprates.⁷ What is more, correlated phases such as anomalous Hall ferromagnetism^{8,9} and quantum Hall effect^{10,11} have been predicted and observed, and are moreover linked to non-trivial Chern numbers.^{12–14}

The observed superconductivity (SC) is often attributed to the presence of electron pairing mechanisms that yield broken-symmetry states^{15–18} and strange-metal behavior,^{19–22} but also electron-phonon pairing has been discussed.^{23,24} Similar correlation effects and robust SC were further observed in twisted N -layer graphene for $2 \leq N \leq 5$.²⁵ Notably, in the case $N = 3$, a Pauli limit violation by a factor of 3 was seen,^{26–28} reinforcing the idea that the SC in these layered systems is indeed unconventional.^{29–32}

The competition between different symmetry breaking patterns is difficult to address due to the emergent $U(4)$ symmetry realized by the electron system in the strong coupling limit.^{33–41} Even though these moiré systems seem to be well-controlled compared to e.g. cuprates as they can be electrically doped, there is still no consensus on the precise phase diagram that should depend sensitively on the surrounding dielectric environment.^{21,42} This could explain that STM measurements show Kekulé patterns in the electron density,^{43,44} while former experiments in a different setup with two metallic gates have given evidence of a nematic phase.⁴⁵

We will undertake the precise determination of the phase diagram of TBG by applying a self-consistent Hartree-Fock method in real space, including all the re-

mote bands of the system. This microscopic real space implementation represents a key advantage, as the different phases turn out to be very sensitive to the on-site Hubbard repulsion, which otherwise cannot be disentangled from the long-range Coulomb interaction in momentum space.

Taking into account all the remote bands is also a must to discern the competition among states whose energy difference is sometimes below 0.1 meV. For this purpose, we will resort to a slight simplification and consider magic angle TBG under hydrostatic pressure at a larger twist angle.⁴⁶ This is in the spirit of the continuum model⁴, where there is a single dimensionless coupling with a critical value at the flat-band regime, therefore making possible to trade larger moiré unit cells by smaller ones, at the cost of decreasing the interlayer distance. This is confirmed by the fact that SC can be tuned experimentally by applying hydrostatic pressure (thereby reducing the interlayer distance).⁴⁷

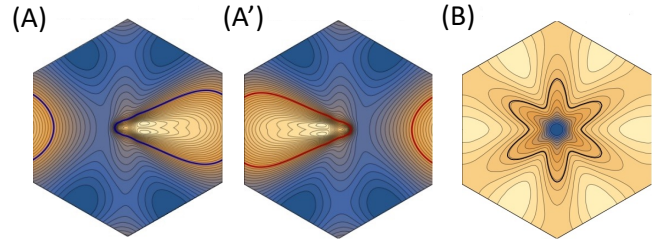


FIG. 1. Energy contour maps showing the Fermi lines in the second valence band for (A) spin-up and (A') spin-down electrons in the moiré Brillouin zone of TBG with twist angle $\theta \approx 3.5^\circ$ under hydrostatic pressure, for interaction strength $\alpha = 0.1 \text{ eV} \times a$ ($a/\sqrt{3}$ being the C-C distance) and filling fraction of 2.4 holes per moiré unit cell. (B) Energy contour map showing the Fermi line in the second conduction band for the same interaction strength and filling fraction of 2.3 electrons per moiré unit cell. Contiguous contour lines differ by a constant step of 0.5 meV, from lower energies in blue to higher energies in light color.

We will show that, in the hole-doped regime relevant for SC, there is a quantum critical point separating the

strong-coupling regime of the Coulomb interaction, with an intervalley-coherent ground state, and the intermediate coupling regime where the ground state is instead valley polarized. Most significantly, this quantum phase transition implies a change in the symmetry of the bands, which are C_6 -invariant in the strong-coupling side, but only invariant under reflection by a mirror plane for larger dielectric screening, as shown in Fig. 1. Indeed, this latter regime is consistent with the observations of nematicity in the experiments of Ref. 28, while the intervalley coherence in strong coupling would be compatible with the STM experiments reported in Refs. 43, 44, and 48.

Our microscopic approach displays also a strong particle-hole asymmetry in the weak coupling regime, since the phase diagram in the electron-doped regime relevant for SC has a single dominant phase, with a C_6 -invariant intervalley-coherent ground state, as seen in Fig. 1. We arrive then at the prediction that the SC should have different character in the hole-doped and the electron-doped regimes of TBG. In the hole-doped nematic regime, the Fermi line has a reflection plane but no inversion symmetry. This leads to Ising SC with spin-valley locking, by which the two spin projections in a Cooper pair belong to opposite valleys and Fermi lines. On the electron-doped regime, the SC becomes more standard as the two spin projections of the Cooper pair share the same C_6 -symmetric Fermi line, though we will see that unconventional order parameters arise from the strong anisotropy of the e - e interaction.

Tight-binding Hamiltonian. We consider twisted bilayer graphene under hydrostatic pressure for the magic twist angle condition at $\theta = 3.5^\circ$ whose band structure is similar to the one at $\theta = 1.16^\circ$ without pressure, see the Supplemental Material.⁴⁹ The non-interacting tight-binding Hamiltonian reads

$$H_0 = - \sum_{n,m} \sum_{i,j} \sum_{\sigma} t_{n,m}^{i,j} \psi_{n,i,\sigma}^\dagger \psi_{m,j,\sigma}, \quad (1)$$

where the hopping matrix element $t_{n,m}^{i,j}$ only depends on the distance between lattice sites, i.e., $t_{n,m}^{i,j} = t(|\mathbf{R}_n - \mathbf{R}_m + \boldsymbol{\delta}_i - \boldsymbol{\delta}_j|)$ with \mathbf{R}_n denoting the lattice vector of unit cell n and $\boldsymbol{\delta}_i$ the position of lattice site i with respect to the unit cell. The spin is labeled by σ . We use the Slater-Koster parametrization

$$t(\mathbf{r}) = V_{pp\pi} e^{\frac{a_0 - r}{r_0}} \left(1 - \left(\frac{\mathbf{r} \cdot \mathbf{e}_z}{r} \right)^2 \right) + V_{pp\sigma} e^{\frac{d_\perp^0 - r}{r_0}} \left(\frac{\mathbf{r} \cdot \mathbf{e}_z}{r} \right)^2,$$

where $a_0 = 1.42\text{\AA}$ is the C-C distance, $r_0 = 0.319a_0$ the decay parameter, and $d_\perp^0 = 3.34\text{\AA}$ denotes the equilibrium interlayer distance. Due to the layered structure, the projection $\mathbf{r} \cdot \mathbf{e}_z$ is either zero or $d_\perp = \frac{1}{1.134}d_\perp^0$, the interlayer distance of the compressed lattice for $\theta = 3.48^\circ$. Further, we set $V_{pp\pi} = 2.7\text{eV}$ and $V_{pp\sigma} = 0.48\text{eV}$.⁵⁰

Coulomb interaction. The total Hamiltonian shall be written as $H = H_0 + H_{\text{int}}$ where the interaction term is

split into a long-ranged Coulomb interaction and a short-ranged on-site Hubbard term, $H_{\text{int}} = H_V + H_U$:

$$H_V = \frac{1}{2} \sum_{n,m} \sum_{i,j} \sum_{\sigma,\sigma'} V_{n,m}^{i,j} \psi_{n,i,\sigma}^\dagger \psi_{m,j,\sigma'}^\dagger \psi_{m,j,\sigma'} \psi_{n,i,\sigma}, \quad (2)$$

$$H_U = \frac{U}{2} \sum_{n,i} \sum_{\sigma} \psi_{n,i,\sigma}^\dagger \psi_{n,i,\bar{\sigma}}^\dagger \psi_{n,i,\bar{\sigma}} \psi_{n,i,\sigma}, \quad (3)$$

where $\bar{\sigma}$ denotes the opposite spin-projection. Again, the Coulomb potential shall only depend on the distance between lattice sites, $V_{n,m}^{i,j} = v(|\mathbf{R}_n - \mathbf{R}_m + \boldsymbol{\delta}_i - \boldsymbol{\delta}_j|)$, and is implemented by the double-gated potential

$$v(|\mathbf{r}|) = \frac{e^2}{4\pi\epsilon_0\epsilon} \sum_n \frac{(-1)^n}{|\mathbf{r} + n\xi\mathbf{z}|} \xrightarrow{r \gg \xi} \frac{e^2}{4\pi\epsilon_0\epsilon} \frac{2\sqrt{2}e^{-\pi r/\xi}}{\xi\sqrt{r/\xi}}, \quad (4)$$

where ϵ stands for the intrinsic dielectric constant of the system, which we will use as a variable to change the strength of the interaction. Alternatively, we will use $\alpha = e^2/4\pi\epsilon_0\epsilon = \tilde{\alpha} \text{ eV} \times a$ with $a = \sqrt{3}a_0$.

The double-gated potential applies for the experimental setups where two metallic plates are placed at $z = \pm\xi/2$. For large distances, the interaction is thus effectively screened on a distance of ξ/π .⁵¹ We will choose $\xi = 10\text{nm}$, a value consistent with several TBG experiments^{52,53} that needs to be compared to the moiré length $L_M \approx 5\text{nm}$. For the exchange interaction, it then suffices to take into account the central and the 19 surrounding moiré cells. For the direct interaction, more than 100 surrounding moiré cells are included which is numerically less costly. Let us finally note that the final results do not significantly depend on ξ .

Hartree-Fock solution. The interacting system shall be treated within the restricted Hartree-Fock approach, i.e., we will only consider spin-symmetric solutions and the spin-quantum number σ shall be suppressed from now on. The on-site interaction H_U would then only lead to a constant energy shift if there was a homogeneous density distribution. However, already the non-interacting model shows strong localization around the AA-stacked regions and we also find sublattice polarization, each one being three-fold rotationally symmetric. In fact, the final results significantly depend on U which can not easily be discussed within a continuum approach.

We will study the ground-state mainly at integer filling factor $\nu = 0, \pm 2$ for on-site Hubbard interactions $U = 0.5, 4\text{eV}$ and $\epsilon = 12, 15, 20, 30, 60$, corresponding to $\tilde{\alpha} = 0.5, 0.4, 0.3, 0.2, 0.1$. For $\epsilon \approx 100$, there is a phase transition to a gapless phase which will not be addressed here.

The Hartree-Fock equations are solved on the moiré Brillouin zone with a 12×12 grid. For each parameter set (ν, U, ϵ) , we usually perform 600 iterations in order to reach convergence; only close to the phase transition at $(\nu = 0, U = 0.5\text{eV}, \epsilon = 15)$, 2000 iterations are necessary. Moreover, for each parameter set we perform the calculation for ten different initial conditions, see SM. This is

important as the Hartree-Fock equations are non-linear and can lead to more than one stable solution. In fact, for $(\nu = -2, U = 0.5\text{eV}, \epsilon = 60)$, $(\nu = -2, U = 4\text{eV}, \epsilon = 12, 15, 20, 30, 60)$, $(\nu = 2, U = 0.5\text{eV}, \epsilon = 15, 20, 30)$, and $(\nu = 2, U = 4\text{eV}, \epsilon = 15, 20)$, we find two different solutions/phases. Then, the solution with lowest energy is chosen which gives rise to a phase transition at $(\nu = -2, U = 4\text{eV}, \epsilon \approx 20)$ and $(\nu = 2, U = 0.5\text{eV}, \epsilon \approx 20)$, see SM.⁴⁹

For most parameters, the energy bands have already converged after ~ 20 iterations. For the convergence of the order parameters, though, many more iterations are needed. This is due to the emergent symmetry of the ground-state whose band-structure is invariant under a $U(4)$ -rotation.^{33,34,36,38} The self-consistent Hartree-Fock equations thus quickly find the (almost) degenerate manifold of states that spontaneously break the $U(4)$ symmetry, but many additional iterations are necessary to reach the true ground-state. We believe that only within an atomistic tight-binding model, reliable results regarding this symmetry broken state can be obtained.

Reduced density matrix. The Hartree-Fock ground state is characterized by the real-space Hartree-Fock density matrix

$$\rho_{ij}^{HF} = \frac{1}{N_c} \sum_{\epsilon \leq \epsilon_F} \langle \psi_{\mathbf{k},i}^\dagger \psi_{\mathbf{k},j} \rangle, \quad (5)$$

where the subscripts i, j refers to the atom at position δ_i, δ_j in the unit cell, and $\psi_{n,i} = \frac{1}{\sqrt{N_c}} \sum_{\mathbf{k} \in 1.BZ} \psi_{\mathbf{k},i} e^{i\mathbf{k} \cdot \mathbf{R}_n}$ with N_c the number of moiré unit cells and ϵ_F the Fermi energy.

In the continuum limit without spin and for energies close to the Fermi level, the wave function is characterized by four envelope functions for each layer related to sublattice and valley degree of freedom. With \mathbf{K}_ℓ and \mathbf{K}'_ℓ denoting the K -points for each layer, we write the wave function as:

$$|\psi\rangle = \sum_{\ell, \alpha} \sum_{\mathbf{r}_i \in \alpha, \ell} \left[e^{i\mathbf{K}_\ell \cdot \mathbf{r}_i} f_{\alpha, K, \ell}(\mathbf{r}_i) + e^{i\mathbf{K}'_\ell \cdot \mathbf{r}_i} f_{\alpha, K', \ell}(\mathbf{r}_i) \right] |\mathbf{r}_i\rangle,$$

with $\alpha = A, B$ denoting the sublattice and ℓ the layer. This decomposition naturally leads to the density matrix $\rho_{\alpha, \beta, \ell; \alpha', \beta', \ell'}(\mathbf{r}, \mathbf{r}') = f_{\alpha, \beta, \ell}^*(\mathbf{r}) f_{\alpha', \beta', \ell'}(\mathbf{r}')$ that contains all information of the long-wavelength theory, with $\beta = K, K'$. Here, we will mainly discuss a reduced density matrix by integrating, or tracing, over the orbital and layer degrees of freedom,

$$\rho_{\alpha, \beta; \alpha', \beta'} = \int_{A_M} d\mathbf{r} \sum_{\ell} \rho_{\alpha, \beta, \ell; \alpha', \beta', \ell}(\mathbf{r}, \mathbf{r}). \quad (6)$$

As shown in the SM, we can relate the full HF density matrix of Eq. (5) to the reduced local density matrix of Eq. (91) by performing closed loops on the lattice. Finally, we can decompose ρ into hermitian components, $\rho_{\gamma, \delta; \gamma', \delta'} = \sum_{\alpha\beta} \rho_{\alpha, \beta} [\sigma_\alpha \tau_\beta]_{\gamma, \delta; \gamma', \delta'} = \sum_{\alpha\beta} \langle \sigma_\alpha \tau_\beta \rangle [\sigma_\alpha \tau_\beta]_{\gamma, \delta; \gamma', \delta'}$ where

$\sigma_\alpha, \tau_\beta$ denote the Pauli matrices for sublattice and valley degree of freedom including the unity matrix with $\alpha, \beta = 0, 1, 2, 3$.

The algorithm can be used for any hexagonal system that is subjected to a structure much larger than the atomic scale. Also extensions to include layer and spin-degrees of freedom are possible. Moreover, our approach goes beyond the "nearsightedness" of the density matrix coined by Walter Kohn^{54,55} as it only requires the information stored on a local Kekulé unit cell.

Phase diagram. The phase diagram can be characterized by the valley polarized (diagonal order) and intervalley coherent (off-diagonal order) phase whose order parameters assume almost quantized values in their respective phases. The density matrix of Eq. (91) can then be written as

$$\rho = \begin{pmatrix} x(\alpha) & 0 & 0 & a(\alpha)e^{i\varphi_1} \\ 0 & y(\alpha) & b(\alpha)e^{i\varphi_2} & 0 \\ 0 & b(\alpha)e^{-i\varphi_2} & y'(\alpha) & 0 \\ a(\alpha)e^{-i\varphi_1} & 0 & 0 & x'(\alpha) \end{pmatrix}, \quad (7)$$

where approximate expressions of the diagonal and off-diagonal elements are derived in the SM.⁴⁹ For $\nu = 0$, we obtain a pure state with $\rho^2 = \rho$; for $\nu = \pm 2$, the density matrix defines a mixed state.

Valley polarization (VP) only occurs for $\nu = \pm 2$ and the bands are almost completely polarized up to 95%. For smaller twist angles realizing the magic angle condition, this polarization is even increasing and can reach up to 98% for the real magic angle at $\theta \approx 1.05^\circ$. For $\nu = \pm 3$, the lowest conduction band per spin-channel is half-filled and the occupied states are again almost fully valley polarized with up to 85%. Only for $\nu = \pm 1$, this (almost) complete polarization is lost.

Intervalley coherence (IVC) occurs predominantly for $\nu = 0$ and the bands are IVC polarized up to 92%. For $\nu = \pm 2$, the order parameter is half the value of charge neutrality, however, we could have defined our order parameter including a factor 2 that would take into account the proper normalization of the initial wave function. Then, the valence band at $\nu = -2$, both valence bands at $\nu = 0$, and the conduction band at $\nu = 2$ are predominantly intervalley coherent (per spin-channel).

Fig. 2 presents a summary of our main results and shows selective order parameters for the different interaction strengths and filling factors. We observe several phase transitions and strong particle-hole asymmetry in the weak coupling regime; in the strong coupling regime, however, particle-hole symmetry is almost completely restored.

In Fig. 3, we show the total gap and the average gap at the K -points as function of the same parameters. For $\nu = \pm 2$, the gap is always topological with Chern number $|C| = 1$ per spin channel. This needs to be contrasted with the gap at charge neutrality that is considerable larger and always trivial with $C = 0$.

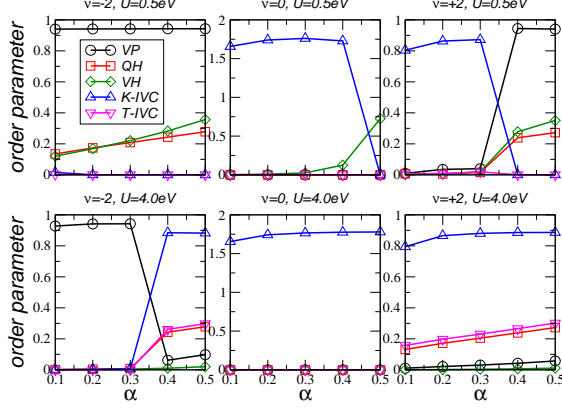


FIG. 2. Phase diagrams of magic angle twisted bilayer graphene for integer filling factors $\nu = -2$ (left), $\nu = 0$ (center), and $\nu = 2$ (right) and Hubbard on-site interaction $U = 0.5\text{eV}$ (upper panels) and $U = 4\text{eV}$ (lower panels) as function of the coupling strength $\alpha = \frac{e^2}{4\pi\epsilon_0\epsilon}$ in units of $\text{eV} \times a$. The phases are characterized by the order parameters for valley polarization (τ_z) (VP), quantum Hall ($\langle\sigma_z\tau_z\rangle$) (QH), valley Hall ($\langle\sigma_z\rangle$) (VH), Kramers intervalley coherence $|\langle\sigma_y\tau_{x/y}\rangle|$ (K-IVC), and T -symmetric intervalley coherence $|\langle\sigma_x\tau_{x/y}\rangle|$ (T-IVC), see SM.

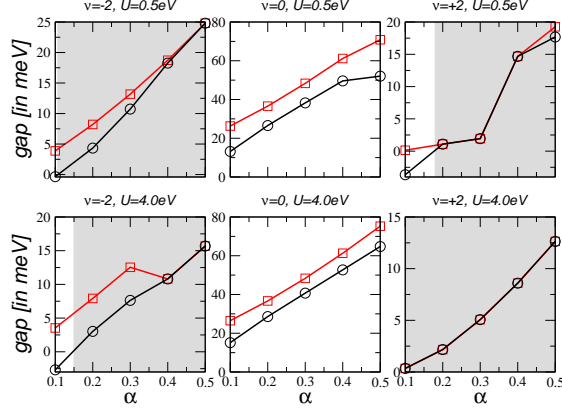


FIG. 3. The total gap (black triangles) and the average gap at the K -points (red squares) of the correlator insulator phase for integer filling factors $\nu = -2$ (left), $\nu = 0$ (center), and $\nu = 2$ (right) and Hubbard on-site interaction $U = 0.5\text{eV}$ (upper panels) and $U = 4\text{eV}$ (lower panels) as function of the coupling strength $\alpha = \frac{e^2}{4\pi\epsilon_0\epsilon}$ in units of $\text{eV} \times a$. The shaded region indicates a topological gap with Chern number $|C| = 1$ (for one spin-channel).

Mesoscopic wave function. At charge neutrality, we find valley coherence in form of a pure state with $\rho^2 = \rho$. The density matrix can be well approximated by $\rho_{\text{KIVC}} =$

$|\varphi\rangle\langle\varphi|$ where $|\varphi\rangle$ denotes the K-IVC state.^{36,49} We can then make the following separation ansatz for the envelope wave functions, valid on the moiré unit cell:

$$|\psi(\mathbf{r})\rangle = \phi(\mathbf{r})|\varphi\rangle, \quad (8)$$

with $|\psi(\mathbf{r})\rangle = (f_{A,K}(\mathbf{r}), f_{B,K}(\mathbf{r}), f_{A,K'}(\mathbf{r}), f_{B,K'}(\mathbf{r}))^T$ and summation over ℓ is implied. Furthermore, $\phi(\mathbf{r}) \sim \exp(-\xi|\mathbf{r}|^2/L_M^2)$ with $\xi \sim 3$ which confines the wave function around the AA -stacked regions centred at $\mathbf{r} = 0$. This is in line with the heavy-fermion model for TBG.⁵⁶

Nematicity. For $(\nu = -2, U = 4\text{eV}, \epsilon = 60, 30, 20)$ and $(\nu = 2, U = 0.5\text{eV}, \epsilon = 60, 30, 20)$, the band structure lacks C_3 symmetry and only displays one mirror symmetry. Interestingly, the reduced density matrix does then not depend on ϵ and simply reads $\rho = \frac{1}{2}\mathcal{P}_K$ and $\rho = \frac{1}{2}(\mathbf{1} + \rho_{\text{KIVC}})$, respectively, where \mathcal{P}_K denotes the projection operator on valley K . This is in line with Refs. 21 and 42. This universality of the *even* density matrix of Eq. (91) has to be contrasted to the *odd* density matrix for which the contributions of the two layers are subtracted, see SM.⁴⁹

Superconductivity. We will now discuss the pairing instability of the ground-state in the weak coupling regime $\epsilon \sim 60$ and for $U = 4\text{eV}$ which should be a realistic value in twisted bilayer graphene.^{57,58} This demands the analysis of the Cooper pair vertex V for electrons with zero total momentum.^{59,60} The vertex can be parameterized in terms of the angles ϕ and ϕ' of the respective momenta of spin-up incoming and outgoing electrons at given energy ϵ . The instabilities of the vertex show up by solving the equation encoding the iteration of the scattering of Cooper pairs

$$V(\phi, \phi') = V_0(\phi, \phi') - \frac{1}{(2\pi)^2} \int_0^{\Lambda_0} \frac{d\epsilon}{\epsilon} \int_0^{2\pi} d\phi'' \frac{\partial k_{\perp}}{\partial \epsilon} \frac{\partial k_{\parallel}}{\partial \phi''} V_0(\phi, \phi'') V(\phi'', \phi'), \quad (9)$$

where k_{\parallel}, k_{\perp} are the longitudinal and transverse components of the momentum for each energy contour line while $V_0(\phi, \phi')$ is the bare vertex at a high-energy cutoff Λ_0 .

Eq. (9) can be simplified by differentiating with respect to the cutoff which leads to

$$\epsilon \frac{\partial \widehat{V}(\phi, \phi')}{\partial \epsilon} = \frac{1}{2\pi} \int_0^{2\pi} d\phi'' \widehat{V}(\phi, \phi'') \widehat{V}(\phi'', \phi'), \quad (10)$$

with $\widehat{V}(\phi, \phi') = F(\phi)F(\phi')V(\phi, \phi')$ and $F(\phi) = \sqrt{(\partial k_{\perp}/\partial \epsilon)(\partial k_{\parallel}/\partial \phi)/2\pi}$. Eq. (10) implies that the vertex is a function of the variable ϵ/Λ_0 . If the initial condition $V_0(\phi, \phi')$ has a negative eigenvalue for any of its harmonics projected onto the Fermi line, the solution of Eq. (10) will display a divergence at a critical energy scale ϵ_c as $\epsilon \rightarrow 0$, i.e., the signature of the pairing instability given by

$$\epsilon_c = \Lambda_0 e^{-1/|\lambda|}, \quad (11)$$

Eigenvalue λ	harmonics	Irr. Rep.
2.12	1	
0.51	$\sin(\phi)$	A''
0.38	$\cos(\phi)$	A'
-0.19	$\sin(4\phi)$	A''
0.18	$\sin(2\phi)$	A''
-0.12	$\cos(6\phi)$	A'

TABLE I. Eigenvalues of the Cooper-pair vertex with largest magnitude and dominant harmonics grouped according to the irreducible representations of the approximate C_h symmetry, for the Fermi lines as shown in Fig. 1 (A) and (A') .

Eigenvalue λ	harmonics	Irr. Rep.
3.47	1	
0.89	$\{\cos(\phi), \sin(\phi)\}$	E_2
0.82		
0.30	$\{\cos(2\phi), \sin(2\phi)\}$	E_1
0.29		
0.18	$\sin(3\phi)$	B_2
-0.17	$\cos(3\phi)$	B_1

TABLE II. Eigenvalues of the Cooper-pair vertex with largest magnitude and dominant harmonics grouped according to the irreducible representations of the approximate C_{6v} symmetry, for the Fermi line as shown in Fig. 1 (B).

where λ denotes the negative eigenvalue and Λ_0 the effective band width. The initial vertex $V_0(\phi, \phi')$ at the high-energy cutoff is dressed by the iteration of particle-hole scattering processes

$$V_0(\phi, \phi') = v_{\mathbf{k}-\mathbf{k}'} + \frac{\bar{v}^2 \tilde{\chi}_{\mathbf{k}+\mathbf{k}'}}{1 - \bar{v} \tilde{\chi}_{\mathbf{k}+\mathbf{k}'}} , \quad (12)$$

where \mathbf{k}, \mathbf{k}' are the respective momenta for angles ϕ, ϕ' , \bar{v} is the average potential in momentum space (≈ 5 meV $\times a^2$), and $\tilde{\chi}_{\mathbf{q}}$ denotes the particle-hole susceptibility.^{32,61} The final step is to project the vertex onto the harmonics $\cos(n\phi), \sin(n\phi)$ which build up the different contributions to $\hat{V}(\phi, \phi')$ at the high-energy cutoff.

We have carried out this operation along the Fermi lines of our model at filling fraction $\nu = -2.4$ shown in Fig. 1 (A) and (A') and at filling fraction $\nu = 2.3$ shown in Fig. 1 (B). The eigenvalues for the different harmonics can be grouped according to the irreducible representations of the approximate symmetry groups C_h and C_{6v} , respectively.

The results are shown in Tables I and II. In both cases, there is a negative coupling with relatively large

magnitude $|\lambda| \approx 0.19$ and $|\lambda| \approx 0.17$, respectively, leading to a divergence in that channel at the energy scale of Eq. (11). In TBG, the magnitude of Λ_0 is constrained by the reduced bandwidth of the second valence and conduction bands, respectively, as shown in Fig. 1. We can assign to Λ_0 the value of half the bandwidth, so that $\Lambda_0 \sim 10$ meV. This leads to a critical temperature $T_c \sim 1$ K in both cases. However, the nature of the superconducting pairing is very different. Since the bands at $\nu = -2.4$ are nematic and spin-split, we predict Ising SC similarly to what happens in twisted trilayer graphene.³² For $\nu = 2.3$, the bands are spin-degenerate and due to the odd pairing function with irrep B_1 , the spinor-wave function needs to transform as a triplet state.

Summary and Conclusions. We have discussed TBG structures under hydrostatic pressure that display flat bands and competition between different symmetry breaking patterns. In order to estimate the full effect of the long-ranged and short-ranged electron-electron interaction, an exact self-consistent real-space Hartree-Fock approach has been used including all remote bands. Moreover, we have introduced order parameters defined with respect to a reduced density matrix of the interacting system.

Notably, for the normal state at 2-hole doping and $U = 4$ eV, we find a valley polarized state with nematicity for weak coupling as observed in Ref. 28. At 2-electron doping, we find a mixed intervalley coherent state with T -symmetric IVC components that give rise to a Kekulé charge-density wave order for strong coupling as observed in Refs. 43, 44, and 48. At charge neutrality, we find a pure K-IVC state that should be phase-disordered beyond the moiré scale.

For the superconducting phase, we expect SC only in the weak-coupling regime, as for the strong-coupling regime the Fermi line becomes more and more isotropic and thus no strong pairing-instability can develop. Moreover, we predict Ising SC for hole-doping and conventional triplet Cooper-pairing for electron doping in the weak coupling. This can be tested by induced spin-orbit coupling by proximity which would enhance the critical temperature only in the hole-doped regime as done in Bernal bilayer graphene.^{62,63}

Acknowledgement. The work was supported by grant PID2020-113164GB-I00 funded by MCIN/AEI/10.13039/501100011033 as well as by the CSIC Research Platform on Quantum Technologies PTI-001. The access to computational resources of CESGA (Centro de Supercomputación de Galicia) is also gratefully acknowledged.

SUPPLEMENTAL MATERIAL

I. MICROSCOPIC REAL-SPACE MODEL

We consider commensurate twisted bilayer graphene (TBG) structures with a relative twist angle θ_i , parametrized by an integer i with the formula¹:

$$\cos(\theta_i) = \frac{3i^2 + 3i + \frac{1}{2}}{3i^2 + 3i + 1}. \quad (13)$$

The new basis vectors of the superlattice, in terms of the previous basis $\{\mathbf{a}_1, \mathbf{a}_2\}$ are

$$\mathbf{t}_1 = i\mathbf{a}_1 + (i+1)\mathbf{a}_2 \quad \mathbf{t}_2 = -(i+1)\mathbf{a}_1 + (2i+1)\mathbf{a}_2, \quad (14)$$

moreover, the number of sites inside a moiré unit cell is also given in terms of i

$$N = 4((i+1)^2 + i^2 + i(i+1)), \quad (15)$$

and the new lattice constant can be calculated with:

$$L_M = \sqrt{3i^2 + 3i + 1}a, \quad (16)$$

with a being the graphene's lattice constant, $a \approx 0.246 \text{ nm}$.

To make contact to actual TBG experiments, the system will be placed between two metallic gates, each at a distance $\xi/2$ to the bilayer. This additional consideration will be relevant when considering the effect of electron-electron interactions, since it will induce an external screening in the otherwise bare Coulomb potential.

According to our previous remarks, the real first magic angle is then given by $i = 31$ under ambient conditions. In our calculations we find that the bands become remarkably flat for $i = 28$ ($\theta \sim 1.16$) within the non-interacting tight-binding model Hamiltonian H_0 , defined in Section 2.1. The reason for this discrepancy is the absence of in-plane relaxation in our model which notably alters the general shape of the bands at small twist angles⁵⁰. For smaller twist angles, though, in-plane relaxation can be neglected and we will use $i = 28$ as our benchmark for the first magic angle of equilibrium TBG.

In this paper, we consider a TBG structure with $i = 9$ ($\theta_9 \sim 3.48^\circ$) with a modified reduced interlayer distance achieved by applying hydrostatic pressure of the GPa order (see⁴⁶ for numerical details on the required pressures) perpendicular to the plane of the crystal. In particular, we require a reduction of $d_{\perp,9} = \frac{1}{1.134}d_{\perp}^0$ with the equilibrium interlayer distance for of turbostratic graphene being $d_{\perp}^0 = 3.34\text{\AA}$ to achieve flat bands near CNP similar to those of $i = 28$.

For comparison, in Figure 4 we show the band structures of $i = 9$ and $i = 28$ calculated under a real space tight-binding scheme with no electron-electron interactions (see Eq. (6) in Sec. 2.1). It can be seen that in both cases, the bandwidth E_W in the ΓK high-symmetry line is of the order of a few meV, and so we can expect electron correlations to play an important role due to the Coulomb potential being of the same order as the kinetic energy, i.e. $E_W \sim \frac{e^2}{4\pi\epsilon_0\epsilon L_M}$ with ϵ being the permittivity of the system and e the charge of the electron. Typical moire lattice constants for these structures are of the order of 13 nm. However, exerting pressure, the moire lattice scale may become considerably smaller of the order of 5 nm.

Let us finally note that we obtain almost identical bands and correlated insulator phases also for $i = 12$ ($\theta_{12} \sim 2.64^\circ$) with interlayer reduction $d_{\perp,12} = \frac{1}{1.095}d_{\perp}^0$. Our results should thus also closely resemble the phase diagram of magic angle bilayer graphene under ambient pressure.

A. Hartree-Fock theory

In the main text, the general Hamiltonian H was written as the sum of a non-interacting Hamiltonian H_0 and a term H_{int} containing the Hubbard and Coulomb interactions

$$H = H_0 + H_{\text{int}}. \quad (17)$$

The tight-binding Hamiltonian reads

$$H_0 = - \sum_{n,m} \sum_{i,j} \sum_{\sigma} t_{n,m}^{i,j} \psi_{n,i,\sigma}^{\dagger} \psi_{m,j,\sigma} \quad (18)$$

where the n, m run over different unit cell, i, j run over the different lattice sites within the unit cell and σ denotes the spin projection. We assume that the hopping matrix element $t_{n,m}^{i,j}$ depends on the distance between lattice sites,

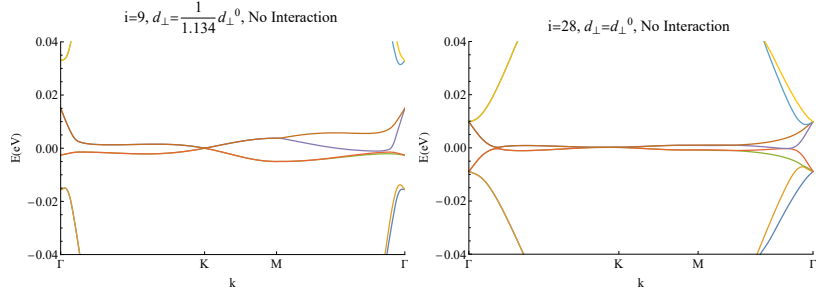


FIG. 4. Low energy bands for $i = 9$ and $i = 28$ calculated using a free real space tight-binding model without $e^- - e^-$ interaction. For $i = 9$, a modified interlayer distance has been used. Both, the general shape and the flatness are remarkably similar in all cases. Here we take $d_{\perp}^0 = 3.34 \text{ \AA}$, the equilibrium interlayer distance for AB stacking in TBG.

i.e., $t_{n,m}^{i,j} = t(|\mathbf{R}_n - \mathbf{R}_m + \boldsymbol{\delta}_i - \boldsymbol{\delta}_j|)$ where \mathbf{R}_n denotes the lattice vector of unit cell n and $\boldsymbol{\delta}_i$ the position of lattice site i with respect to the unit cell.

The Coulomb interaction is given by

$$H_{int} = \frac{1}{2} \sum_{n,m} \sum_{i,j} \sum_{\sigma,\sigma'} V_{n,m}^{i,j} \psi_{n,i,\sigma}^{\dagger} \psi_{m,j,\sigma'}^{\dagger} \psi_{m,j,\sigma'} \psi_{n,i,\sigma} . \quad (19)$$

Again, the interaction potential shall only depend on the distance between lattice sites, i.e., $V_{n,m}^{i,j} = V(|\mathbf{R}_n - \mathbf{R}_m + \boldsymbol{\delta}_i - \boldsymbol{\delta}_j|)$. We will further split the interaction term into a long-ranged Coulomb interaction and a short-ranged on-site Hubbard term to avoid singularities. We therefore have $H_{int} = H_V + H_U$ with

$$H_V = \frac{1}{2} \sum_{n,m} \sum_{i,j} \sum_{\sigma,\sigma'} V_{n,m}^{i,j} \psi_{n,i,\sigma}^{\dagger} \psi_{m,j,\sigma'}^{\dagger} \psi_{m,j,\sigma'} \psi_{n,i,\sigma} , \quad (20)$$

$$H_U = \frac{U}{2} \sum_{n,i} \sum_{\sigma} \psi_{n,i,\sigma}^{\dagger} \psi_{n,i,\bar{\sigma}}^{\dagger} \psi_{n,i,\bar{\sigma}} \psi_{n,i,\sigma} , \quad (21)$$

where $\bar{\sigma}$ denotes the opposite spin-projection to σ .

We can now perform a Fourier transform by

$$\psi_{n,i,\sigma} = \frac{1}{\sqrt{N_c}} \sum_{\mathbf{k} \in 1.BZ} \psi_{\mathbf{k},i,\sigma} e^{i\mathbf{k}(\mathbf{R}_n + \zeta \boldsymbol{\delta}_i)} , \quad (22)$$

where N_c is the number of unit cells. For sake of generality, we included an additional phase within the unit cell which is characterized by the position $\boldsymbol{\delta}_i$ of lattice site i if we set $\zeta = 1$. However, ζ can also be set to zero such there is the same phase for the whole unit cell.

We now define new variables by $\mathbf{R}_{\ell} = \mathbf{R}_n - \mathbf{R}_m$ and $\tilde{\mathbf{R}}_p = \frac{1}{2}(\mathbf{R}_n + \mathbf{R}_m)$. The factor $\frac{1}{2}$ guarantees that the Jacobian of the mapping is norm-conserving and by choosing periodic boundary conditions, there are no finite size effects to take care of. We can thus replace $\sum_{n,m} \rightarrow \sum_{\ell,p}$ and since the hopping matrix element and the Coulomb potential only depend on \mathbf{R}_{ℓ} , i.e., $t_{n,m}^{i,j} \rightarrow t_{\ell}^{i,j}$ and $V_{n,m}^{i,j} \rightarrow V_{\ell}^{i,j} = V(\mathbf{R}_{\ell} + \boldsymbol{\delta}_i - \boldsymbol{\delta}_j)$, we can use the following identity ($\tilde{\mathbf{R}}_p = \frac{1}{2} \mathbf{R}_p$):

$$\frac{1}{N_c} \sum_p e^{-i\frac{\mathbf{R}_p}{2}(\mathbf{k}-\mathbf{k}')} = \delta_{\mathbf{k},\mathbf{k}'+2\mathbf{G}} , \quad (23)$$

where \mathbf{G} denotes a reciprocal lattice vector. Since the sum of the wave vectors is confined to the first Brillouin zone, there are no Umklapp processes to be taken care of. The interaction hamiltonian thus reads

$$H_V = \frac{1}{2} \sum_{\ell} \sum_{i,j} V_{\ell}^{i,j} \frac{1}{N_c} \sum_{\mathbf{k},\mathbf{k}'} \sum_{\sigma,\sigma'} \psi_{\mathbf{k},i,\sigma}^{\dagger} \psi_{\mathbf{k}',j,\sigma}^{\dagger} \psi_{\mathbf{k}',j,\sigma'} \psi_{\mathbf{k},i,\sigma} , \quad (24)$$

$$H_U = \frac{U}{2} \sum_{\ell} \sum_i \frac{1}{N_c} \sum_{\mathbf{k},\mathbf{k}'} \sum_{\sigma} \psi_{\mathbf{k},i,\sigma}^{\dagger} \psi_{\mathbf{k}',i,\bar{\sigma}}^{\dagger} \psi_{\mathbf{k}',i,\bar{\sigma}} \psi_{\mathbf{k},i,\sigma} . \quad (25)$$

With the Hartree-Fock approximation, we thus have the following effective one-particle Hamilton operator $H^{HF} = H_0 + H_V^{HF} + H_U^{HF}$ with:

$$H_0 = - \sum_{\ell; i, j} t_\ell^{i, j} \sum_{\mathbf{k}, \sigma} \psi_{\mathbf{k}, i, \sigma}^\dagger \psi_{\mathbf{k}, j, \sigma} e^{-i\mathbf{k}(\mathbf{R}_\ell + \delta_i - \delta_j)} \quad (26)$$

$$H_V^{HF} = \sum_\ell \sum_{i, j} V_\ell^{i, j} \left[\langle \mathcal{O}_H^j \rangle \mathcal{O}_H^i - \sum_\sigma \langle \mathcal{O}_F^{\ell, i, j, \sigma, \sigma} \rangle^* \mathcal{O}_F^{\ell, i, j, \sigma, \sigma} \right] \quad (27)$$

$$H_U^{HF} = \frac{U}{N_c} \sum_i \sum_\sigma \psi_{\mathbf{k}, i, \sigma}^\dagger \psi_{\mathbf{k}, i, \sigma} \langle \psi_{\mathbf{k}, i, \bar{\sigma}}^\dagger \psi_{\mathbf{k}, i, \bar{\sigma}} \rangle. \quad (28)$$

In the Hartree-Fock decoupling we have assumed translation invariance, i.e., $\langle \psi_{\mathbf{k}, i, \sigma}^\dagger \psi_{\mathbf{k}', j, \sigma'} \rangle = 0$ if $\mathbf{k} \neq \mathbf{k}'$, and constrained the spin structure to be diagonal, i.e., $\langle \psi_{\mathbf{k}, i, \sigma}^\dagger \psi_{\mathbf{k}, j, \bar{\sigma}} \rangle = 0$. The operators \mathcal{O}_H^i and $\mathcal{O}_F^{\ell, i, j, \sigma, \sigma'}$ are defined by

$$\mathcal{O}_H^i = \frac{1}{\sqrt{N_c}} \sum_{\mathbf{k}, \sigma} \psi_{\mathbf{k}, i, \sigma}^\dagger \psi_{\mathbf{k}, i, \sigma}, \quad (29)$$

$$\mathcal{O}_F^{\ell, i, j, \sigma, \sigma'} = \frac{1}{\sqrt{N_c}} \sum_{\mathbf{k}} \psi_{\mathbf{k}, i, \sigma}^\dagger \psi_{\mathbf{k}, j, \sigma'} e^{-i\mathbf{k}(\mathbf{R}_\ell + \delta_i - \delta_j)}. \quad (30)$$

The ground-state energy is given by

$$E_0 = E_{kin} + \frac{1}{2} E_{Hartree} + \frac{1}{2} E_{Fock} + \frac{1}{2} E_U. \quad (31)$$

where we defined the kinetic, Fock, and Hartree energy:

$$E_{kin} = - \sum_{\ell; i, j} t_\ell^{i, j} \sum_{\mathbf{k}, \sigma} \langle \psi_{\mathbf{k}, i, \sigma}^\dagger \psi_{\mathbf{k}, j, \sigma} \rangle e^{-i\mathbf{k}(\mathbf{R}_\ell + \delta_i - \delta_j)} \quad (32)$$

$$E_{Fock} = - \sum_{\ell; i, j} V_\ell^{i, j} \sum_\sigma |\langle \mathcal{O}_F^{\ell, i, j, \sigma, \sigma} \rangle|^2 \quad (33)$$

$$E_{Hartree} = \sum_{\ell; i, j} V_\ell^{i, j} \langle \mathcal{O}_H^i \rangle \langle \mathcal{O}_H^j \rangle \quad (34)$$

$$E_U = \frac{U}{N_c} \sum_i \sum_{\mathbf{k}, \sigma} \langle \psi_{\mathbf{k}, i, \sigma}^\dagger \psi_{\mathbf{k}, i, \sigma} \rangle \langle \psi_{\mathbf{k}, i, \bar{\sigma}}^\dagger \psi_{\mathbf{k}, i, \bar{\sigma}} \rangle \quad (35)$$

In the following we will discuss the energy density per particle $E/A_M/N$, with $A_M = \frac{3}{2}a^2\sqrt{3i^2 + 3i + 1}$ the area of the moiré lattice and N the total number of electrons in the system, or simply the energy per particle E/N .

B. Roothaan equations

The self-consistent Hartree-Fock equations are also called Roothaan equations which can be written as a (generalized) eigenvalue problem

$$F[\psi]\psi = \epsilon\psi \quad (36)$$

where F denotes the so-called Fock matrix which depends on the wave functions ψ . ψ shall denote the matrix of the eigenfunctions, and ϵ is the diagonal matrix of orbital energies. It is a set of nonlinear equation and the Fock matrix F is actually an approximation of the true Hamiltonian operator of the quantum system, i.e., $F = H^{HF} \approx H$. It includes the effects of electron-electron repulsion only on an average level and because the Fock operator is a one-electron operator, it does not include the electron correlation energy.

This set of non-linear equations cannot be uniquely solved and might even possess several solutions. We will solve it iteratively by starting from a particular density distribution n_i where the atomic positions $i = (\alpha, \ell)$ shall be parameterized by sublattice $\alpha = A, B$ and layer $\ell = 1, 2$. We thus have $n_i = n_0 + \delta n_i$ where $n_0 = 1/2$ is the density of the neutral system and $\delta n_i = 0.1\xi_i$. With $\xi_i = \mathcal{O}(1)$, we make sure that the system is pushed far from equilibrium.

We consider four cases $\xi_{A,1} = \xi_{B,1} = \xi_{A,1} = \xi_{B,1} = 1$, $\xi_{A,1} = -\xi_{B,1} = \xi_{A,1} = -\xi_{B,1} = 1$, $\xi_{A,1} = -\xi_{B,1} = -\xi_{A,1} = \xi_{B,1} = 1$, and $\xi_{A,1} = \xi_{B,1} = -\xi_{A,1} = -\xi_{B,1} = 1$. We also consider the symmetric case with negative sign $n_i = n_0 + 0.2(0.5 - \xi)$ and $\xi = 1$. The initial condition can further be generalized by using arbitrary densities, but including the same sublattice and layer (im)balances, i.e., $\xi_i \in [0, 1]$ is now a random number which gives another five initial conditions.

After the first iteration, we adjust the chemical potential such that $\sum_i n_i = 1/2 + \nu/A_M$ with A_M the area of the moiré unit cell. Depending on the filling factor and interaction strength, we may obtain more than one solution. We then choose the one with lower energy. This procedure also allows us to extract the energy difference between different phases.

II. REDUCED DENSITY MATRIX

In the main text, we introduce the reduced density matrix

$$\rho_{\alpha,\beta;\alpha',\beta'} = \int_{A_M} d\mathbf{r} \sum_{\ell} f_{\alpha,\beta,\ell}^*(\mathbf{r}) f_{\alpha',\beta',\ell}(\mathbf{r}). \quad (37)$$

We can decompose ρ into Hermitian components, $\rho_{\gamma,\delta;\gamma',\delta'} = \sum_{\alpha\beta} \rho_{\alpha,\beta} [\sigma_{\alpha}\tau_{\beta}]_{\gamma,\delta;\gamma',\delta'} = \sum_{\alpha\beta} \langle \sigma_{\alpha}\tau_{\beta} \rangle [\sigma_{\alpha}\tau_{\beta}]_{\gamma,\delta;\gamma',\delta'}$ where $\sigma_{\alpha}, \tau_{\beta}$ denote the Pauli matrices for sublattice and valley degree of freedom including the unity matrix with $\alpha, \beta = 0, x, y, z$. The expectation values of the sixteen generators that define the $SU(4)$ symmetry group can be grouped into four categories.

The first one describes intra-sublattice and intra-valley terms. They read

$$\langle 1 \rangle = \rho_{AK,AK} + \rho_{BK,BK} + \rho_{AK',AK'} + \rho_{BK',BK'}, \quad (38)$$

$$\langle \sigma_z \rangle = \rho_{AK,AK} - \rho_{BK,BK} + \rho_{AK',AK'} - \rho_{BK',BK'}, \quad (39)$$

$$\langle \tau_z \rangle = \rho_{AK,AK} + \rho_{BK,BK} - \rho_{AK',AK'} - \rho_{BK',BK'}, \quad (40)$$

$$\langle \sigma_z \tau_z \rangle = \rho_{AK,AK} - \rho_{BK,BK} - \rho_{AK',AK'} + \rho_{BK',BK'}. \quad (41)$$

The second group describes intra-sublattice and inter-valley terms. They read

$$\langle \sigma_x \rangle = 2 \operatorname{Re}(\rho_{AK,BK} + \rho_{AK',BK'}), \quad (42)$$

$$\langle \sigma_y \rangle = 2 \operatorname{Im}(\rho_{AK,BK} + \rho_{AK',BK'}), \quad (43)$$

$$\langle \sigma_x \tau_z \rangle = 2 \operatorname{Re}(\rho_{AK,BK} - \rho_{AK',BK'}), \quad (44)$$

$$\langle \sigma_y \tau_z \rangle = 2 \operatorname{Im}(\rho_{AK,BK} - \rho_{AK',BK'}). \quad (45)$$

The third group describes inter-sublattice and intra-valley terms. They read

$$\langle \tau_x \rangle = 2 \operatorname{Re}(\rho_{AK,AK'} + \rho_{BK,BK'}), \quad (46)$$

$$\langle \tau_y \rangle = 2 \operatorname{Im}(\rho_{AK,AK'} + \rho_{BK,BK'}), \quad (47)$$

$$\langle \sigma_z \tau_x \rangle = 2 \operatorname{Re}(\rho_{AK,AK'} - \rho_{BK,BK'}), \quad (48)$$

$$\langle \sigma_z \tau_y \rangle = 2 \operatorname{Im}(\rho_{AK,AK'} - \rho_{BK,BK'}). \quad (49)$$

The last group describes inter-sublattice and inter-valley terms. They read

$$\langle \sigma_x \tau_x \rangle = 2 \operatorname{Re}(\rho_{AK,BK'} + \rho_{BK,AK'}), \quad (50)$$

$$\langle \sigma_x \tau_y \rangle = 2 \operatorname{Im}(\rho_{AK,BK'} + \rho_{BK,AK'}), \quad (51)$$

$$\langle \sigma_y \tau_x \rangle = 2 \operatorname{Im}(\rho_{AK,BK'} - \rho_{BK,AK'}), \quad (52)$$

$$\langle \sigma_y \tau_y \rangle = -2 \operatorname{Re}(\rho_{AK,BK'} - \rho_{BK,AK'}). \quad (53)$$

In the main text, we discuss the order parameters related to valley polarization $\langle \tau_z \rangle$, valley Hall effect $\langle \sigma_z \rangle$, and quantum Hall effect $\langle \sigma_z \tau_z \rangle$. Moreover, we discuss the order parameter for Kramers intervalley coherence $|\langle \sigma_x \tau_{x/y} \rangle| \equiv \sqrt{\langle \sigma_x \tau_x \rangle^2 + \langle \sigma_x \tau_y \rangle^2}$ and time-reversal invariant intervalley coherence $|\langle \sigma_x \tau_{x/y} \rangle| \equiv \sqrt{\langle \sigma_y \tau_x \rangle^2 + \langle \sigma_y \tau_y \rangle^2}$.

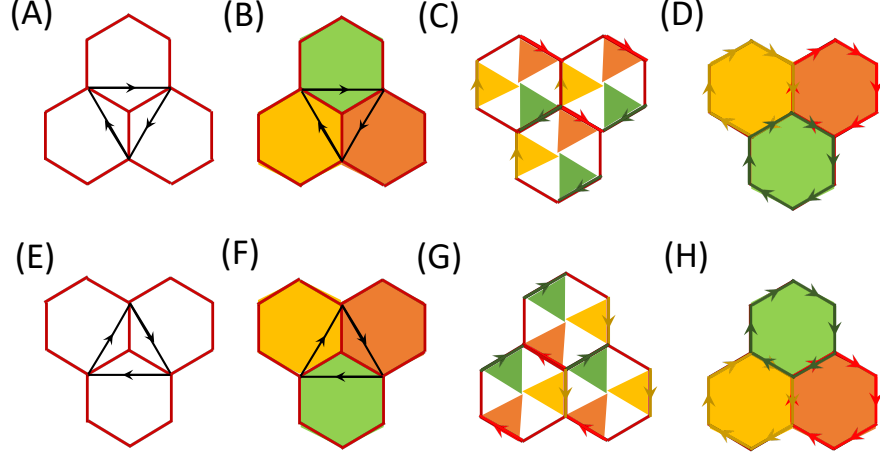


FIG. 5. Triangular and hexagonal loops on the lattice in order to determine the valley order parameters. (A) and (B) show the triangular loop on the A-sublattice, yielding intra-sublattice contributions; (C) and (D) shows the three hexagonal loops with the central atom belonging to the A-sublattice, yielding inter-sublattice contributions. The different colors stand for additional phases $e^{i2n\pi/3}$ with $n = 0$ (green), $n = 1$ (yellow), and $n = 2$ (red). The corresponding loops of (E), (F), (G), and (H) are related to the B-sublattice.

III. ORDER PARAMETERS FOR A LATTICE MODEL

We will now generate the reduced density matrix from the real-space density matrix. For this, we fix the geometry of single layer graphene. To simplify the discussion, our analysis will be the same for the two layers which is a good approximation for small twist angles. However, one can easily introduce the relative rotation which would refine our results.

The hexagonal lattice shall be described by two basis vectors $\mathbf{a}_1 = a_0(\sqrt{3}/2, 3/2)$, $\mathbf{a}_2 = a_0(-\sqrt{3}/2, 3/2)$ with $a_0 = 1.42\text{\AA}$. The nearest neighbour sites are defined by $\boldsymbol{\delta}_1 = a_0(\sqrt{3}/2, -1/2)$, $\boldsymbol{\delta}_2 = a_0(0, 1)$, $\boldsymbol{\delta}_0 = \boldsymbol{\delta}_3 = a_0(-\sqrt{3}/2, -1/2)$. The Brillouin zone is spanned by $\mathbf{b}_1 = \frac{2\pi}{3a_0}(1, \sqrt{3})$ and $\mathbf{b}_2 = \frac{2\pi}{3a_0}(-1, \sqrt{3})$ that defines the two K -points $\mathbf{K} = (\frac{4\pi}{3\sqrt{3}}a_0, 0)$ and $\mathbf{K}' = -\mathbf{K}$.

In order to derive the long-wavelength coefficients, we will use $e^{i\mathbf{K}\pm\cdot\mathbf{a}} = e^{\pm i\frac{2\pi}{3}}$ with $\mathbf{a} = \mathbf{a}_1, \mathbf{a}_2 - \mathbf{a}_1, -\mathbf{a}_2$ and $e^{\pm i\mathbf{K}\cdot\boldsymbol{\delta}_1} + e^{\pm i\mathbf{K}\cdot\boldsymbol{\delta}_2} + e^{\pm i\mathbf{K}\cdot\boldsymbol{\delta}_3} = 0$ which is simplified to $\sum_{n=0,1,2} e^{in\frac{2\pi}{3}} = 0$.

In the long-wavelength limit, the wave function can be separated into a fast oscillating part and a slowly oscillating envelope function. A typical wave function contains contributions from both valleys and our tight-binding model differentiates between A- and B-sublattice. We will thus make for the general wave function $|\psi\rangle = \sum_{\mathbf{r}_i} \psi(\mathbf{r}_i)|\mathbf{r}_i\rangle$ the following ansatz which discriminates sublattice as well as valley degree of freedom:

$$|\psi\rangle = \sum_{\mathbf{r}_i \in A} [e^{i\mathbf{K}\cdot\mathbf{r}_i} f_{AK}(\mathbf{r}_i) + e^{-i\mathbf{K}\cdot\mathbf{r}_i} f_{AK'}(\mathbf{r}_i)] |\mathbf{r}_i\rangle + \sum_{\mathbf{r}_i \in B} [e^{i\mathbf{K}\cdot\mathbf{r}_i} f_{BK}(\mathbf{r}_i) + e^{-i\mathbf{K}\cdot\mathbf{r}_i} f_{BK'}(\mathbf{r}_i)] |\mathbf{r}_i\rangle \quad (54)$$

The envelope function $f_{\alpha,\beta}$ will be smooth on the moiré scale, and we will approximate

$$f_{\alpha,\beta}(\mathbf{r} + \mathbf{a}) = f_{\alpha,\beta}(\mathbf{r}) + \mathcal{O}(a/L_M). \quad (55)$$

We can now perform suitable loops on the lattice that will yield the components of the reduced density matrix, see Fig. 5. This components can be grouped in four categories and involve overlap functions of the form $\psi^*(\mathbf{r})\psi(\mathbf{r} + \mathbf{a})$. They are a property of the initial wave function $|\psi\rangle$ and the expression is thus gauge-invariant since the global phase of $|\psi\rangle$ drops out.

A. Intra-sublattice, intravalley channel

To define the order parameters of the intra-sublattice, intra-valley channel within the tight-binding model, we define the flux through the triangle that is defined by the three adjacent atoms of the same sublattice:

$$\Delta_{++}(\mathbf{r}_i) = \sum_{n=0,1,2} \psi^*(\mathbf{r}_i \pm \boldsymbol{\delta}_n) \psi(\mathbf{r}_i \pm \boldsymbol{\delta}_{n+1}), \quad (56)$$

where the upper sign refers to $\mathbf{r}_i \in B$, the lower sign to $\mathbf{r}_i \in A$. This yields the following expressions:

$$\rho_{AK,AK} = \frac{1}{\sqrt{3}} \sum_{\mathbf{r}_i \in B} (-\text{Re } \Delta_{++}(\mathbf{r}_i) - \text{Im } \Delta_{++}(\mathbf{r}_i)) \quad (57)$$

$$\rho_{AK',AK'} = \frac{1}{\sqrt{3}} \sum_{\mathbf{r}_i \in B} (-\text{Re } \Delta_{++}(\mathbf{r}_i) + \text{Im } \Delta_{++}(\mathbf{r}_i)) \quad (58)$$

$$\rho_{BK,BK} = \frac{1}{\sqrt{3}} \sum_{\mathbf{r}_i \in A} (-\text{Re } \Delta_{++}(\mathbf{r}_i) + \text{Im } \Delta_{++}(\mathbf{r}_i)) \quad (59)$$

$$\rho_{BK',BK'} = \frac{1}{\sqrt{3}} \sum_{\mathbf{r}_i \in A} (-\text{Re } \Delta_{++}(\mathbf{r}_i) - \text{Im } \Delta_{++}(\mathbf{r}_i)) \quad (60)$$

B. Intra-sublattice, intervalley channel

In order to discuss the valley coherent phases within the tight-binding model, we need to consider the triangular flux dressed by three phases that transform as the non-trivial representation of C_3 . For \mathbf{r}_0 on the A -sublattice (+) or B -sublattice (-), we have

$$\Delta_{+-}^\lambda(\mathbf{r}_i) = \sum_{n=0,1,2} e^{\lambda i(n-1)2\pi/3} \psi^*(\mathbf{r}_i \pm \boldsymbol{\delta}_n) \psi(\mathbf{r}_i \pm \boldsymbol{\delta}_{n+1}), \quad (61)$$

where again the upper sign refers to $\mathbf{r}_i \in B$, the lower sign to $\mathbf{r}_i \in A$ and $\lambda = \pm$.

This yields the following expressions:

$$\text{Re } \rho_{AK,AK'} = \frac{1}{\sqrt{3}} \sum_{\mathbf{r}_i \in B} (-\text{Re } \Delta_{+-}^+(\mathbf{r}_i) - \text{Re } \Delta_{+-}^-(\mathbf{r}_i)) \quad (62)$$

$$\text{Im } \rho_{AK,AK'} = \frac{1}{\sqrt{3}} \sum_{\mathbf{r}_i \in B} (-\text{Re } \Delta_{++}^+(\mathbf{r}_i) + \text{Re } \Delta_{++}^-(\mathbf{r}_i)) \quad (63)$$

$$\text{Re } \rho_{BK,BK'} = \frac{1}{\sqrt{3}} \sum_{\mathbf{r}_i \in A} (-\text{Re } \Delta_{++}^+(\mathbf{r}_i) - \text{Re } \Delta_{++}^-(\mathbf{r}_i)) \quad (64)$$

$$\text{Im } \rho_{BK,BK'} = \frac{1}{\sqrt{3}} \sum_{\mathbf{r}_i \in A} (-\text{Re } \Delta_{++}^+(\mathbf{r}_i) + \text{Re } \Delta_{++}^-(\mathbf{r}_i)) \quad (65)$$

C. Inter-sublattice, intravalley channel

To define an order parameter for the valley-coherence based on a tight-binding model, we will start from the general wave function $|\psi\rangle = \sum_{\mathbf{r}_i} \psi(\mathbf{r}_i) |\mathbf{r}_i\rangle$. We now define the following quantity related to the flux around a hexagon via the sum of the six overlap functions:

$$\Delta_{-+}^{1\lambda}(\mathbf{r}_i) = \alpha^\lambda \psi^*(\mathbf{r}_i) \psi(\mathbf{r}_i \pm \boldsymbol{\delta}_2) + \psi^*(\mathbf{r}_i \pm \mathbf{a}_1) \psi(\mathbf{r}_i \pm \mathbf{a}_1 \mp \boldsymbol{\delta}_1) + \alpha^{-\lambda} \psi^*(\mathbf{r}_i \pm \mathbf{a}_1 \mp \mathbf{a}_2) \psi(\mathbf{r}_i \pm \mathbf{a}_1 \mp \mathbf{a}_2 \pm \boldsymbol{\delta}_3) \quad (66)$$

$$\Delta_{-+}^{2\lambda}(\mathbf{r}_i) = \psi^*(\mathbf{r}_i) \psi(\mathbf{r}_i \pm \boldsymbol{\delta}_1) + \alpha^{-\lambda} \psi^*(\mathbf{r}_i \mp \mathbf{a}_2) \psi(\mathbf{r}_i \mp \mathbf{a}_2 \mp \boldsymbol{\delta}_3) + \alpha^\lambda \psi^*(\mathbf{r}_i \mp \mathbf{a}_1) \psi(\mathbf{r}_i \mp \mathbf{a}_1 \pm \boldsymbol{\delta}_2) \quad (67)$$

$$\Delta_{-+}^{3\lambda}(\mathbf{r}_i) = \alpha^{-\lambda} \psi^*(\mathbf{r}_i) \psi(\mathbf{r}_i \pm \boldsymbol{\delta}_3) + \alpha^\lambda \psi^*(\mathbf{r}_i \mp \mathbf{a}_1 \pm \mathbf{a}_2) \psi(\mathbf{r}_i \mp \mathbf{a}_1 \pm \mathbf{a}_2 \pm \boldsymbol{\delta}_2) + \psi^*(\mathbf{r}_i \pm \mathbf{a}_2) \psi(\mathbf{r}_i \pm \mathbf{a}_2 \pm \boldsymbol{\delta}_1) \quad (68)$$

where again the upper sign refers to $\mathbf{r}_i \in A$, the lower sign to $\mathbf{r}_i \in B$ and $\alpha = \exp(-i\frac{2\pi}{3})$ with $\lambda = \pm$. Note that the three phases are identical up to a phase determined by \mathbf{r}_i . Now summing over every third lattice site A^Δ and B^Δ , we obtain

$$\rho_{AK,BK} = \sum_{n=1,2,3} \left(\sum_{\mathbf{r}_i \in A^\Delta} + \sum_{\mathbf{r}_i \in B^\Delta} \right) \Delta_{-+}^{n+}(\mathbf{r}_i), \quad (69)$$

$$\rho_{AK',BK'} = \sum_{n=1,2,3} \left(\sum_{\mathbf{r}_i \in A^\Delta} + \sum_{\mathbf{r}_i \in B^\Delta} \right) \Delta_{-+}^{n+}(\mathbf{r}_i). \quad (70)$$

D. Interband, intervalley channel

We now define the flux around a hexagon via the sum of the six overlap functions:

$$\begin{aligned} \Delta_{--}^1(\mathbf{r}_i) = & \psi^*(\mathbf{r}_i)\psi(\mathbf{r}_i \pm \delta_2) + \psi^*(\mathbf{r}_i \pm \delta_2)\psi(\mathbf{r}_i \pm \mathbf{a}_1) + \psi^*(\mathbf{r}_i \pm \mathbf{a}_1)\psi(\mathbf{r}_i \pm \mathbf{a}_1 \pm \delta_1) \\ & + \psi^*(\mathbf{r}_i \pm \mathbf{a}_1 \pm \delta_1)\psi(\mathbf{r}_i \pm \mathbf{a}_1 \mp \mathbf{a}_2) + \psi^*(\mathbf{r}_i \pm \mathbf{a}_1 \mp \mathbf{a}_2)\psi(\mathbf{r}_i \pm \delta_1) + \psi^*(\mathbf{r}_i \pm \delta_1)\psi(\mathbf{r}_i) \end{aligned} \quad (71)$$

where again the upper sign refers to $\mathbf{r}_i \in A$, the lower sign to $\mathbf{r}_i \in B$. There are intravalley and intervalley contributions, however, the intravalley contribution vanishes due to the node of the Dirac dispersion at the K -point. The intervalley contribution is defined by 3+3 phases which turn out to be the same due to the threefold symmetry. With $\alpha = e^{-i2\pi/3}$, we then obtain

$$\frac{1}{3}\Delta_{--}^1 = e^{-i2\mathbf{K}\cdot\mathbf{r}_0} f_{AK}^* f_{BK'} + e^{i2\mathbf{K}\cdot\mathbf{r}_0} f_{AK'}^* f_{BK} + \alpha e^{-i2\mathbf{K}\cdot\mathbf{r}_0} f_{BK}^* f_{AK'} + \alpha^* e^{i2\mathbf{K}\cdot\mathbf{r}_0} f_{BK'}^* f_{AK}. \quad (72)$$

The oscillating factor $e^{\pm 2i\mathbf{K}\cdot\mathbf{r}_i}$ will give rise to a tripled unit cell since with $\mathbf{r}_i = n_1\mathbf{a}_1 + n_2\mathbf{a}_2$ we have $e^{2i\mathbf{K}\cdot\mathbf{r}_i} = e^{-2\pi i(n_2 - n_1)/3}$. We can thus define the following three inequivalent quantities related to \mathbf{r}_i :

$$\Delta_{--}^1 = 3(x + \alpha^*x^* + y + \alpha y^*) \quad (73)$$

$$\Delta_{--}^2 = 3((x + x^*)\alpha + (y + y^*)\alpha^*) \quad (74)$$

$$\Delta_{--}^3 = 3(\alpha^*x + x^* + \alpha y + y^*) \quad (75)$$

where $x = f_{AK}^*(\mathbf{r}_i)f_{BK'}(\mathbf{r}_i)$ and $y = f_{AK'}^*(\mathbf{r}_i)f_{BK}(\mathbf{r}_i)$. With $\alpha^*\Delta_{--}^1 + \alpha\Delta_{--}^2 + \Delta_{--}^3 = 9(\alpha^*x + y^*)$ and $\alpha^*(\Delta_{--}^1)^* + \alpha(\Delta_{--}^2)^* + (\Delta_{--}^3)^* = 9(x + \alpha^*y^*)$, we finally obtain

$$\rho_{AK,BK'} = \frac{-i}{\sqrt{3}} \left(\sum_{\mathbf{r}_i \in A^\Delta} + \sum_{\mathbf{r}_i \in B^\Delta} \right) [(\alpha^*\Delta_{--}^1 + \alpha\Delta_{--}^2 + \Delta_{--}^3) - \alpha(\alpha^*(\Delta_{--}^1)^* + \alpha(\Delta_{--}^2)^* + (\Delta_{--}^3)^*)] / 3, \quad (76)$$

$$\rho_{BK,AK'} = \frac{i}{\sqrt{3}} \left(\sum_{\mathbf{r}_i \in A^\Delta} + \sum_{\mathbf{r}_i \in B^\Delta} \right) [\alpha(\alpha^*\Delta_{--}^1 + \alpha\Delta_{--}^2 + \Delta_{--}^3) - (\alpha^*(\Delta_{--}^1)^* + \alpha(\Delta_{--}^2)^* + (\Delta_{--}^3)^*)] / 3. \quad (77)$$

In order to derive the above relations, we used $\Delta_{--}^1 + \Delta_{--}^2 + \Delta_{--}^3 = 0$ which is related to current conservation. We also included a factor 3 due to the sum of only every lattice site.

Let us finally comment on the ambiguity of choosing the point of origin. Consider that $\mathbf{r}_i = n_1\mathbf{a}_1 + n_2\mathbf{a}_2 + \boldsymbol{\delta}$. Then, there is an additional phase $e^{\pm i2\mathbf{K}\cdot\boldsymbol{\delta}}$ and the order parameter computes the wave function products up to a global phase that is precisely the $U(1)$ valley phase of TBG. Also, note that $\boldsymbol{\delta} = \pm\mathbf{a}_1$ amounts to a cyclic permutation of the sublattice labels.

E. Order parameter for the Hartree-Fock theory

We are now in the position to define the order parameter for the tight-binding model based on the Hartree-Fock density matrix

$$\rho_{ij,\sigma}^{HF} = \frac{1}{N_c} \sum_{\sigma} \sum_{\varepsilon \leq \varepsilon_{F,\sigma}} \langle \psi_{\mathbf{k},i,\sigma}^\dagger \psi_{\mathbf{k},j,\sigma} \rangle, \quad (78)$$

where the subscripts i, j refers to the atom at position δ_i, δ_j in the unit cell, with N_c the number of moiré unit cells and $\varepsilon_{F,\sigma}$ the Fermi energy for spin-channel σ . Since we only consider spin-degenerate solutions, we will drop the spin-index σ in the following.

The Hartree-Fock theory describes *non-interacting* electrons and we will relate the many-body HF density matrix ρ_{ij}^{HF} to a one-particle density matrix $\rho_{ij} = \psi_i^* \psi_j$ with $|\psi\rangle \propto \sum_i \psi_i |\mathbf{r}_i\rangle$ where $|\mathbf{r}_i\rangle$ stands for the localized Wannier-orbital at lattice site \mathbf{r}_i .

The density matrix ρ_{ij}^{HF} can thus be interpreted as the hopping amplitude from site j to site i , given by the wave function overlap $\psi_i^* \psi_j$. Furthermore, since the Brillouin zone of the moiré system is small compared to the Brillouin zone of the graphene lattice, there is hardly any \mathbf{k} -dependence and the ansatz of Eq. (54) shall represent a good approximation for states close to the Fermi energy.

Let us finally emphasize that the total density matrix ρ_{ij}^{HF} includes the information of all occupied states, see Eq. (78). However, the procedure described above relies on the decomposition of the wave functions into the two valleys, Eq. (54). This decomposition is only valid for states near charge neutrality and our approach cannot account for states at the bottom of the spectrum.

This is evident from Fig. 6, where the trace of ρ is centered around zero at charge neutrality and not - as might be expected - equal to the number of occupied states. In fact, the trace can even be negative since only non-diagonal matrix elements of ρ_{ij}^{HF} with $i \neq j$ are used in the reduction process. Nevertheless, the states that occupied at the bottom of the Fermi sea should only contribute via a constant background that can be appropriately normalized as shown in the following Section.

IV. NORMALIZATION OF THE DENSITY MATRIX

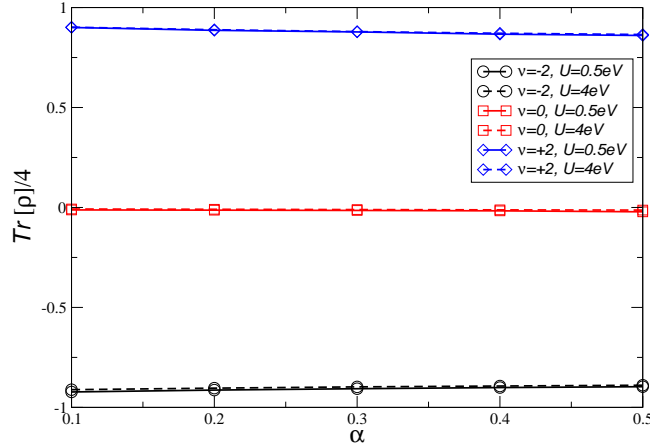


FIG. 6. The trace of the (bare) density matrix ρ as obtained from our algorithm for various integer filling factor, Hubbard on-line interaction, and long-ranged coupling parameter $\alpha = \frac{e^2}{4\pi\epsilon_0\epsilon}$ in units of $eV \times a$.

Let us now analyze the reduced density matrix for the different parameters. In Fig. 6, we show the trace of the density matrix ρ . It depends only on the filling factor ν , up to small deviations, and is centred around zero at charge neutrality. In order to discuss the other 15 components of ρ , we introduce

$$\rho' = \sum_{(\alpha,\beta) \neq (0,0)} \rho_{\alpha,\beta} \sigma_{\alpha} \tau_{\beta}, \quad (79)$$

where $\alpha, \beta = 0, x, y, z$ denote the different Pauli-matrices for sublattice and valley degree of freedom, including the unity matrix. In Fig. 7, we show $\rho'^2 = \rho'^2_{+,+} + \rho'^2_{+,-} + \rho'^2_{-,+} + \rho'^2_{-,-}$ where the four components $\rho'^2_{\nu,\mu}$ refer to the sum of intra-sublattice intra-valley (without the diagonal part indicated by the prime) ($\nu = +, \mu = +$), intra-sublattice inter-valley ($\nu = +, \mu = -$), inter-sublattice intra-valley ($\nu = -, \mu = +$), and inter-sublattice inter-valley ($\nu = -, \mu = -$)

contributions. Again, the absolute value is almost independent of the parameters even though the relative weight changes. Moreover, the weight of $\rho_{-,+}^2$ and especially of $\rho_{+,-}^2$ is negligible. This shall be discussed in more detail in Sec. VI.

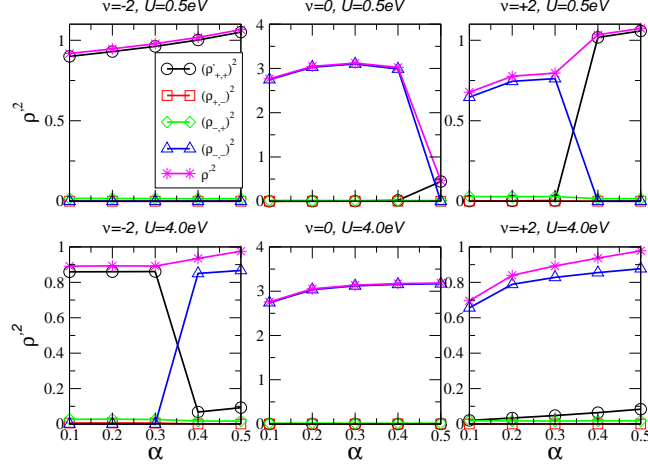


FIG. 7. The weights of the (bare) density matrix ρ' as obtained from our algorithm for various integer filling factors, Hubbard on-line interactions, and long-ranged coupling parameters $\alpha = \frac{e^2}{4\pi\epsilon_0\epsilon}$ in units of $eV \times a$.

Our algorithm should accurately account for the relative weight between the matrix elements. However, since we relate the many-body density matrix to a one-body wave function, we may not expect to get the normalization right. We now define $Q = \lambda\rho$ and add a term proportional to the unity matrix. The normalized density matrix shall thus be given by (we will keep the notation)

$$\rho \rightarrow \frac{1}{2} + Q, \quad (80)$$

For $\nu = \pm 2$, the parameter λ is now chosen such that $\text{Tr} \rho = \frac{4+\nu}{2}$. This sets the normalization of ρ to that of a density matrix for $\frac{4+\nu}{2}$ electrons, i.e. the electrons in the flat bands. For $\nu = 0$, we already have $\text{Tr} \rho \approx 2$, see Fig. 6 and we choose λ such that $Q^2 = 1/4$. As $\rho_{+,-}$ and $\rho_{-,+}$ are almost zero, we will only discuss the diagonal and off-diagonal matrix elements to simplify the discussion. The results are shown in Figs. 8, 9, and 10.

V. DISCUSSION

We are now in the position to discuss the phase diagram via the reduced density matrix.

A. Charge-neutrality point

Let us first discuss the filling factor $\nu = 0$. First, we note that for all parameters we find a pure state with $\rho^2 = \rho$. Even though our normalization of Q and the shift of Eq. (80) allows for a pure state, it is still remarkable as it shows up. For example, if we choose the same normalization $\lambda\rho'^2 = 1/4$ for $\nu = \pm 2$, we do not obtain $\rho^2 = \rho$.

As can be seen from Figs. 8, 9, and 10, the ground-state can be well approximated by a Kramer-intervalley-coherent (K-IVC) state

$$|\Delta\varphi\rangle_{\text{KIVC}} = \frac{1}{\sqrt{2}}(c_1|AK\rangle + e^{i\varphi_1}c_2|BK'\rangle) \otimes \frac{1}{\sqrt{2}}(c_2|BK\rangle + e^{i\varphi_2}c_1|AK'\rangle), \quad (81)$$

with $\rho \approx \rho_{\text{KIVC}} = |\Delta\varphi\rangle\langle\Delta\varphi|$ with $\Delta\varphi = \varphi_1 - \varphi_2 \approx |\pi|$. However, for $\rho^2 = \rho$, all matrix elements must contribute.

For $U = 4eV$, $c_1 = c_2 = 1$ and we have a "pure" valley-coherent state. For $U = 0.5eV$, we only have $c_1c_2 = 1$ and for $\alpha \approx 0.4eV\text{\AA}$, we predict a phase transition to a chiral insulator.

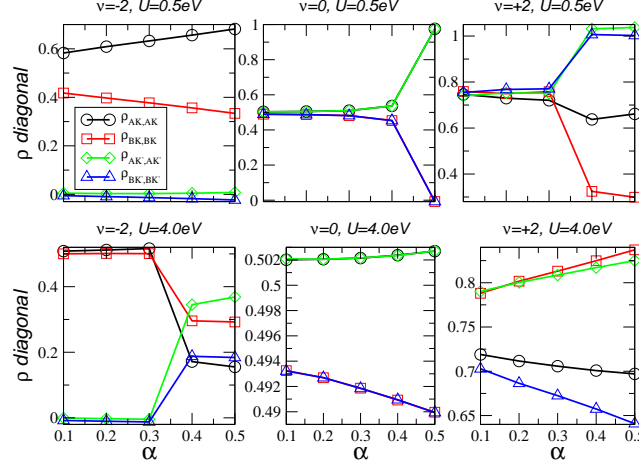


FIG. 8. The diagonal matrix elements of the density matrix as obtained from Eq. (80) for various integer filling factor, Hubbard on-line interaction, and long-ranged coupling parameter $\alpha = \frac{e^2}{4\pi\epsilon_0\epsilon}$ in units of $eV \times a$.

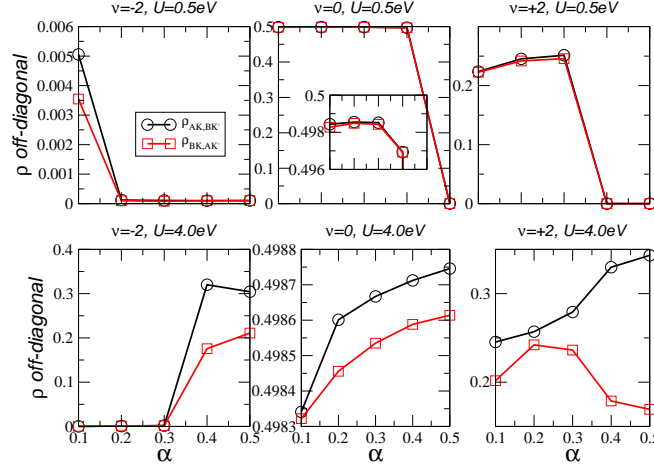


FIG. 9. The absolute values of the off-diagonal matrix elements of the density matrix as obtained from Eq. (80) for various integer filling factor, Hubbard on-line interaction, and long-ranged coupling parameter $\alpha = \frac{e^2}{4\pi\epsilon_0\epsilon}$ in units of $eV \times a$.

B. Hole doping at half-filling

At $\nu = -2$, we find predominately a valley polarized state, i.e., there is no off-diagonal matrix elements. However, it is not a pure state, also by construction.

For $U = 0.5eV$, the diagonal matrix elements for one valley, say K' , are given by $\rho_{XK',XK'} \approx 0$ (the small negative value is within our numerical accuracy). For the diagonal matrix elements of the other valley, we find $\rho_{XK,XK} = \rho_{\pm}^0 \pm c\tilde{\alpha}$ with $\alpha = \tilde{\alpha}eV \times a$ and $c \approx 0.2$ and $\rho_{\pm}^0 \approx 0.5 \pm 0.05$. The upper/lower sign applies for sublattice $X = A/B$.

For $U = 4eV$, we find that the valley polarized state is only the ground-state for $\tilde{\alpha} \leq 0.3$. In this case, we find again for one valley, say K , $\rho_{XK,XK} \approx 0.5$ and for the other valley $\rho_{XK',XK'} \approx 0$.

For $U = 4eV$ and $\tilde{\alpha} \geq 0.4$, we find a valley coherent state with non-zero off-diagonal elements. However, this state

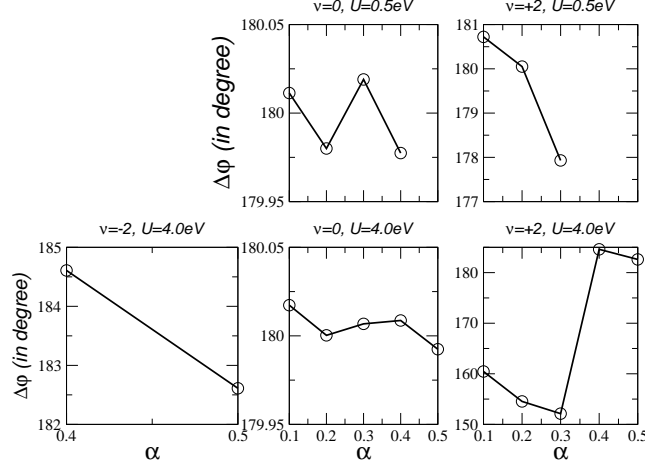


FIG. 10. The phase-difference of the off-diagonal matrix elements of the density matrix as obtained from Eq. (80) for various integer filling factor, Hubbard on-line interaction, and long-ranged coupling parameter $\alpha = \frac{e^2}{4\pi\epsilon_0\epsilon}$ in units of $eV \times a$.

cannot be simply written as a pure state of Eq. (81).

C. Electron doping at half-filling

At $\nu = 2$, we find predominately a valley coherent state, i.e., there are off-diagonal matrix elements. However, it is not a pure state, again also by construction.

For $U = 0.5eV$, we find that the valley coherent state is only the ground-state for $\tilde{\alpha} \leq 0.3$. Even though, it is not the K-IVC pure state of Eq. (81), we can still approximate $\rho = \frac{1}{2}(1 + \rho_{KIVC})$.

For $U = 0.5eV$ and $\tilde{\alpha} \geq 0.4$, we find a valley polarized state with zero off-diagonal elements. We can approximate this state by filling all electrons of one valley, say K' , with $\rho_{XK',XK'} = 1$ and for the diagonal matrix elements of the other valley, we again find $\rho_{XK,XK} = \rho_{\pm}^0 \pm c\tilde{\alpha}$ with $\alpha = \tilde{\alpha}eV \times a$ and $c \approx 0.2$ and $\rho_{\pm}^0 \approx 0.5 \pm 0.05$. The upper/lower sign applies for sublattice $X = A/B$.

For $U = 4eV$, we always find a valley coherent state with non-zero off-diagonal elements. The diagonal matrix elements show a linear behavior in $\tilde{\alpha}$, however, it cannot be associated to the previously identified K-IVC-state. In fact, we expect a phase-transition at for $\alpha \approx 0.3eV \times a$ from a valley coherent state with $\Delta\varphi \neq \pi$ to a valley coherent state with $\Delta\varphi \approx \pi$.

D. Summary

We can now summarize the density matrix for the different parameters.

- $\nu = -2, U = 0.5eV$:

$$\rho = \begin{pmatrix} x(\alpha) & 0 & 0 & 0 \\ 0 & y(\alpha) & 0 & 0 \\ 0 & 0 & 0 & 0 \\ 0 & 0 & 0 & 0 \end{pmatrix}, \quad (82)$$

where $x(\alpha) + y(\alpha) = 1$ and we can approximate $x(\alpha) = 0.56 + 0.21\tilde{\alpha}$ and $y(\alpha) = 0.44 - 0.21\tilde{\alpha}$.

- $\nu = 0, U = 0.5\text{eV}, \tilde{\alpha} \leq 0.4$:

$$\rho = \frac{1}{2} \begin{pmatrix} c_1^2 & 0 & 0 & c_1 c_2 e^{i\varphi} \\ 0 & c_2^2 & c_1 c_2 e^{-i\varphi} & 0 \\ 0 & c_1 c_2 e^{i\varphi} & c_1^2 & 0 \\ c_1 c_2 e^{-i\varphi} & 0 & 0 & c_2^2 \end{pmatrix}, \quad (83)$$

where $c_1 \approx c_2 \approx 1$.

- $\nu = 0, U = 0.5\text{eV}, \tilde{\alpha} \geq 0.4$:

$$\rho = \begin{pmatrix} 1 & 0 & 0 & 0 \\ 0 & 0 & 0 & 0 \\ 0 & 0 & 1 & 0 \\ 0 & 0 & 0 & 0 \end{pmatrix}. \quad (84)$$

- $\nu = 2, U = 0.5\text{eV}, \tilde{\alpha} \leq 0.3$:

$$\rho = \begin{pmatrix} x(\alpha) & 0 & 0 & 0 \\ 0 & y(\alpha) & 0 & 0 \\ 0 & 0 & 1 & 0 \\ 0 & 0 & 0 & 1 \end{pmatrix}, \quad (85)$$

where $x(\alpha) + y(\alpha) = 1$ and we can approximate $x(\alpha) = 0.56 + 0.21\tilde{\alpha}$ and $y(\alpha) = 0.44 - 0.21\tilde{\alpha}$.

- $\nu = 2, U = 0.5\text{eV}, \tilde{\alpha} \geq 0.3$:

$$\rho = \frac{1}{2}\mathbf{1} + \frac{1}{4} \begin{pmatrix} 1 & 0 & 0 & e^{i\varphi} \\ 0 & 1 & e^{-i\varphi} & 0 \\ 0 & e^{i\varphi} & 1 & 0 \\ e^{-i\varphi} & 0 & 0 & 1 \end{pmatrix}. \quad (86)$$

- $\nu = -2, U = 4\text{eV}, \tilde{\alpha} \leq 0.3$:

$$\rho = \frac{1}{2} \begin{pmatrix} 1 & 0 & 0 & 0 \\ 0 & 1 & 0 & 0 \\ 0 & 0 & 0 & 0 \\ 0 & 0 & 0 & 0 \end{pmatrix}, \quad (87)$$

- $\nu = -2, U = 4\text{eV}, \tilde{\alpha} \geq 0.3$:

$$\rho = \begin{pmatrix} x(\alpha) & 0 & 0 & a(\alpha)e^{i\varphi} \\ 0 & 0.3 & b(\alpha)e^{-i\varphi} & 0 \\ 0 & b(\alpha)e^{i\varphi} & y(\alpha) & 0 \\ a(\alpha)e^{-i\varphi} & 0 & 0 & 0.2 \end{pmatrix}, \quad (88)$$

where $x(\alpha) + y(\alpha) = 1/2$ and we can approximate $x(\alpha) = 0.25 - 0.21\tilde{\alpha}$ and $y(\alpha) = 0.25 + 0.21\tilde{\alpha}$. We further approximate $a(\alpha) = 0.4 - 0.2\tilde{\alpha}$ and $b(\alpha) = 0.1 + 0.2\tilde{\alpha}$.

- $\nu = 0, U = 4\text{eV}$:

$$\rho = \frac{1}{2} \begin{pmatrix} 1 & 0 & 0 & e^{i\varphi} \\ 0 & 1 & e^{-i\varphi} & 0 \\ 0 & e^{i\varphi} & 1 & 0 \\ e^{-i\varphi} & 0 & 0 & 1 \end{pmatrix}. \quad (89)$$

- $\nu = 2, U = 4\text{eV}$:

$$\rho = \begin{pmatrix} x(\alpha) & 0 & 0 & a(\alpha)e^{i\varphi_1} \\ 0 & y(\alpha) & b(\alpha)e^{i\varphi_2} & 0 \\ 0 & b(\alpha)e^{-i\varphi_2} & y'(\alpha) & 0 \\ a(\alpha)e^{-i\varphi_1} & 0 & 0 & x'(\alpha) \end{pmatrix}, \quad (90)$$

where $x(\alpha) \approx x'(\alpha) \approx 0.72 - 0.2\tilde{\alpha}$ and $y(\alpha) \approx y'(\alpha) \approx 0.88 + 0.2\tilde{\alpha}$. For $\tilde{\alpha} \leq 0.3$, $a(\alpha) \approx b(\alpha) \approx 0.25$ and $\Delta\varphi(\alpha) \rightarrow 5\pi/6$ for $\tilde{\alpha} \rightarrow 0.3$. For $\tilde{\alpha} \geq 0.3$, $a(\alpha) \approx 0.25 - 0.2\tilde{\alpha}$ and $b(\alpha) \approx 0.25 + 0.2\tilde{\alpha}$ and $\Delta\varphi \approx \pi$.

VI. SUBDOMINANT AND "ODD" ORDER PARAMETERS

In this section, we will briefly discuss the subdominant order parameters which are related to intra-sublattice inter-valley and inter-sublattice intravalley scattering. We will also discuss the "odd" order parameters of these channels as they acquire large values in the nematic phases.

A. Subdominant order parameters

As commented above, the phases can be either characterized by a valley polarized (VP) or intervalley coherent (IVC) order parameter. However, also subdominant order parameter occur in the intra-sublattice inter-valley and inter-sublattice intra-valley channel.

In Fig. (11), we show the absolute values of the order parameters related to intra-sublattice inter-valley and inter-sublattice intra-valley scattering. The largest value is given by $\langle\sigma_x\rangle$ and $\langle\sigma_y\rangle$, respectively; still, it is approximately one order of magnitude lower than the dominant order parameters related to either VP or IVC. Let us finally note that it is adiabatically related to the inter-Chern order parameter recently discussed in Ref. 43.

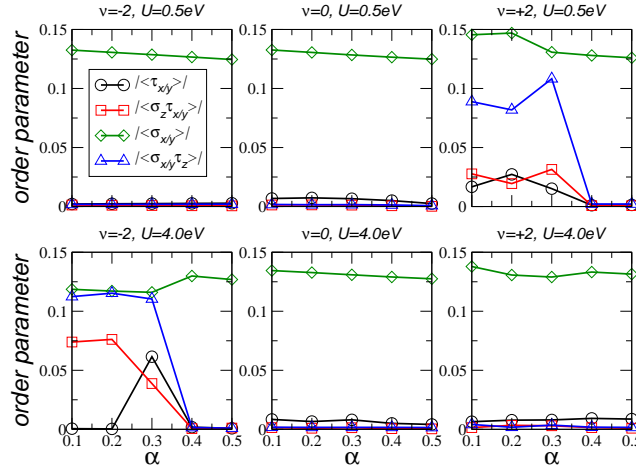


FIG. 11. Absolute values of order parameters related to intra-sublattice inter-valley and inter-sublattice intra-valley scattering for various integer filling factor, Hubbard on-line interaction, and long-ranged coupling parameter $\alpha = \frac{e^2}{4\pi\epsilon_0\epsilon}$ in units of $eV \times a$. In the caption, we abbreviated $|\langle\tau_{x/y}\rangle| = \sqrt{\langle\tau_x\rangle^2 + \langle\tau_y\rangle^2}$, $|\langle\sigma_z\tau_{x/y}\rangle| = \sqrt{\langle\sigma_z\tau_x\rangle^2 + \langle\sigma_z\tau_y\rangle^2}$, $|\langle\sigma_{x/y}\rangle| = \sqrt{\langle\sigma_x\rangle^2 + \langle\sigma_y\rangle^2}$, and $|\langle\sigma_{x/y}\tau_z\rangle| = \sqrt{\langle\sigma_x\tau_z\rangle^2 + \langle\sigma_y\tau_z\rangle^2}$.

B. Dominant "odd" order parameters

Here, we will briefly discuss extensions of the reduced density matrix as discussed in Eq. (91) by discussing the "odd" superpositions of the two layers. We thus define

$$\rho_{\alpha,\beta;\alpha',\beta'}^- = \int_{A_M} d\mathbf{r} \sum_{\ell} (-1)^{\ell-1} f_{\alpha,\beta,\ell}^* (\mathbf{r}) f_{\alpha',\beta',\ell} (\mathbf{r}). \quad (91)$$

This density matrix shall be related to the usual representation $\rho_{\alpha,\beta}^- = \langle\sigma_{\alpha}\tau_{\beta}\eta_z\rangle$ where η_z may be interpreted as the z -component of the Pauli-matrix with respect to the two layers.

In Fig. (12), we show the absolute values of the order parameters related to intra-sublattice inter-valley and inter-sublattice intra-valley scattering of this odd channel. The largest value is given by $\langle\sigma_x\eta_z\rangle$ and $\langle\sigma_y\eta_z\rangle$, respectively, in the phase where there is nematic order. Let us finally note that the corresponding order parameters related to VP and IVC are negligible.

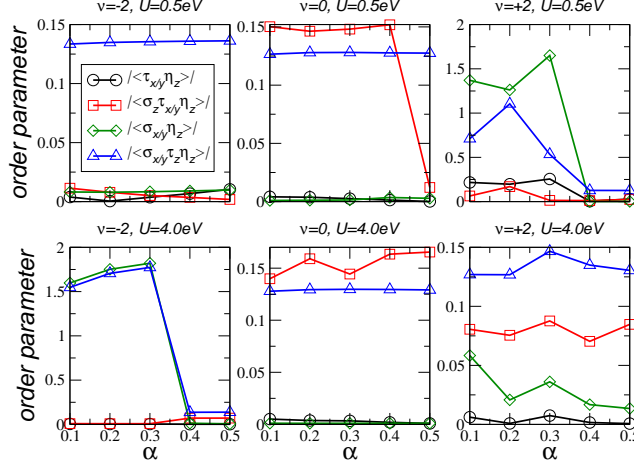


FIG. 12. Absolute values of order parameters related to intra-sublattice inter-valley and inter-sublattice intra-valley scattering and odd layer-superposition for various integer filling factor, Hubbard on-line interaction, and long-ranged coupling parameter $\alpha = \frac{e^2}{4\pi\epsilon_0\epsilon}$ in units of $\text{eV} \times a$. In the caption, we abbreviated $|\langle \tau_{x/y} \eta_z \rangle| = \sqrt{\langle \tau_x \eta_z \rangle^2 + \langle \tau_y \eta_z \rangle^2}$, $|\langle \sigma_z \tau_{x/y} \eta_z \rangle| = \sqrt{\langle \sigma_z \tau_x \eta_z \rangle^2 + \langle \sigma_z \tau_y \eta_z \rangle^2}$, $|\langle \sigma_{x/y} \eta_z \rangle| = \sqrt{\langle \sigma_x \eta_z \rangle^2 + \langle \sigma_y \eta_z \rangle^2}$, and $|\langle \sigma_{x/y} \tau_z \eta_z \rangle| = \sqrt{\langle \sigma_x \tau_z \eta_z \rangle^2 + \langle \sigma_y \tau_z \eta_z \rangle^2}$.

VII. GROUND-STATE ENERGIES AND PHASE TRANSITIONS

We observe several phase transitions, however, the only "real" phase transition occurs for $\nu = 0$, $U = 0.5\text{eV}$ and $\alpha = 0.4\text{eV} \times a$. The other phase transitions result due to a competition between the valley polarized (VP) and inter-valley coherent (IVC) phase, both being a stable solution.

Both phases emerge for different initial conditions and we choose the one with lower total energy. In the tables below, we list the total energy difference $\Delta E = E_{VP} - E_{IVC}$ for the parameters where we find the two phases. We also list the energy difference for the kinetic energy E_{kin} , the Fock and Hartree energy E_{Fock} and $E_{Hartree}$ in units of $\tilde{\alpha}$, and finally the Hubbard energy E_U in units of \tilde{U} , where we introduced the dimensional quantities $\tilde{\alpha}$ and \tilde{U} by $\alpha = \tilde{\alpha}\text{eV} \times a$ and $U = \tilde{U}\text{eV}$. For $\nu = -2$ and $U = 4.0\text{eV}$ as well as for $\nu = 2$ and $U = 0.5\text{eV}$, there is a sign change for ΔE and thus a phase transition from valley polarized to valley coherent and valley coherent to valley polarized, respectively.

$\Delta E = E_{VP} - E_{IVC}$ in meV for $\nu = -2$, $U = 0.5\text{eV}$					
α in $\text{eV} \times a$	ΔE	ΔE_{kin}	$\Delta E_{Fock}/\tilde{\alpha}$	$\Delta E_{Hartree}/\tilde{\alpha}$	$\Delta E_U/\tilde{U}$
0.1	-0.001	-0.001	0.025	0.061	0.006

$\Delta E = E_{VP} - E_{IVC}$ in meV for $\nu = -2$, $U = 4.0\text{eV}$					
α in $\text{eV} \times a$	ΔE	ΔE_{kin}	$\Delta E_{Fock}/\tilde{\alpha}$	$\Delta E_{Hartree}/\tilde{\alpha}$	$\Delta E_U/\tilde{U}$
0.1	-0.147	+0.0285	+2.302	+1.933	-0.266
0.2	-0.099	+0.124	-0.230	+1.279	-0.214
0.3	-0.027	+0.018	+0.693	+0.881	-0.201
0.4	+0.131	-0.146	+1.783	+0.459	-0.191
0.5	+0.365	-0.308	+2.614	-0.619	-0.086

$\Delta E = E_{VP} - E_{IVC}$ in meV for $\nu = 2$, $U = 0.5\text{eV}$					
α in $\text{eV} \times a$	ΔE	ΔE_{kin}	$\Delta E_{Fock}/\tilde{\alpha}$	$\Delta E_{Hartree}/\tilde{\alpha}$	$\Delta E_U/\tilde{U}$
0.2	+0.240	+0.176	+1.776	-5.826	+0.460
0.3	+0.030	+0.356	+1.200	-8.336	+0.834
0.4	-0.438	+0.424	-0.518	-5.656	+0.212

$\Delta E = E_{VP} - E_{IVC}$ in meV for $\nu = 2$, $U = 4.0\text{eV}$					
α in $\text{eV} \times a$	ΔE	ΔE_{kin}	$\Delta E_{Fock}/\tilde{\alpha}$	$\Delta E_{Hartree}/\tilde{\alpha}$	$\Delta E_U/U$
0.2	+0.050	+0.193	-0.009	+1.091	-0.222
0.3	+0.149	+0.059	+1.481	+0.087	-0.213

VIII. RENORMALIZED BAND STRUCTURES

Here, we present some typical Hartree-Fock bands along the high symmetry lines. In Fig. 28 and 14, the bands are shown for filling factor $\nu = -2$. In all cases, there is one split-band indicated by the blue curve. However, also other remote valence bands may contribute for filling factors below $\nu = -2$.

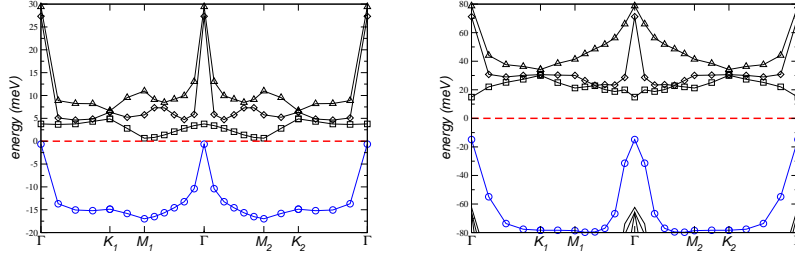


FIG. 13. Hartree Fock bands for $\nu = -2$ and $U = 0.5\text{eV}$ at $\epsilon = 60$ (left) and $\epsilon = 12$ (right). The chemical potential is set to zero and indicated by the red dashed line.

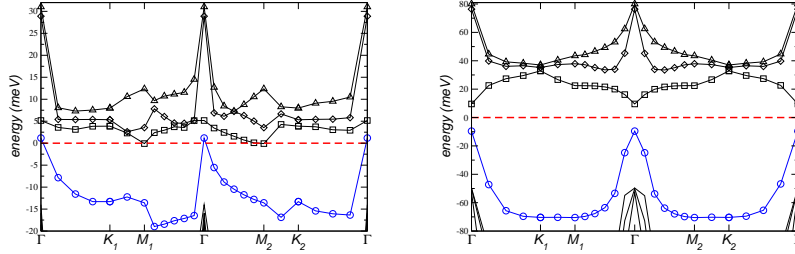


FIG. 14. Hartree Fock bands for $\nu = -2$ and $U = 4.0\text{eV}$ at $\epsilon = 60$ (left) and $\epsilon = 12$ (right). The chemical potential is set to zero and indicated by the red dashed line.

In Fig. 15 and 16, the bands are shown for filling factor $\nu = 2$. Again, in all cases there is one split-band indicated by the blue curve. In contrary to hole-doping, other remote conduction bands do not contribute for filling factors above $\nu = 2$.

The bands for $\nu = -2$ and $\nu = 2$ do not display an obvious many-body particle-hole symmetry. Nevertheless, the phase diagram recovers the particle-hole symmetry in the strong-coupling limit. This is due to the fact that the interaction term which is particle-hole symmetric, becomes more dominant relative to the kinetic term which breaks the particle hole symmetry.

Generally, the gap at $\nu = \pm 2$ is topological with Chern number $|C| = 1$. This changes at charge neutrality and where the gap becomes trivial. The band structure is shown in Figs. 17 and 18.

IX. RENORMALIZED CONTOUR PLOTS

Here, we present some typical contour plots for the Hartree-Fock bands. In Fig. 19 and 20, the bands are shown for filling factor $\nu = -2$. The relative orientation is arbitrary.

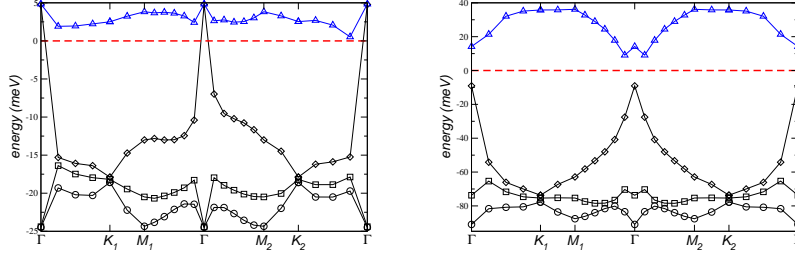


FIG. 15. Hartree Fock bands for $\nu = 2$ and $U = 0.5\text{eV}$ at $\epsilon = 60$ (left) and $\epsilon = 12$ (right). The chemical potential is set to zero and indicated by the red dashed line.

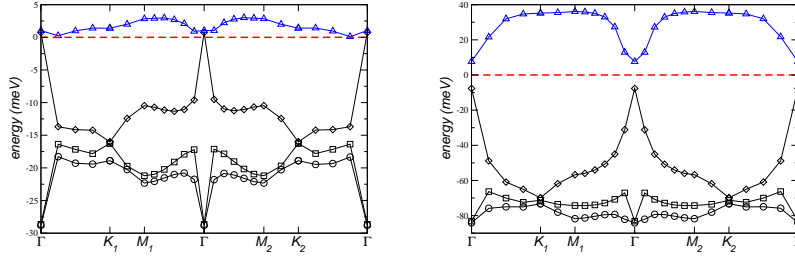


FIG. 16. Hartree Fock bands for $\nu = 2$ and $U = 4.0\text{eV}$ at $\epsilon = 60$ (left) and $\epsilon = 12$ (right). The chemical potential is set to zero and indicated by the red dashed line.

In Fig. 21 and 22, the bands are shown for filling factor $\nu = 2$. Also here, the relative orientation is arbitrary.

Remarkably, there is a breaking of the C_3 -symmetry for $n = -2$, $U = 4\text{eV}$ and $n = 2$, $U = 0.5\text{eV}$. In both cases, this symmetry is recovered if we set the onsite energy $U = 0$. Also if we set $\alpha = 0$ and U finite, there is no symmetry breaking. This nematic state is thus due to an interplay of long-ranged and short-ranged interaction. Interestingly, this state generates an order parameter $\sigma_{x,y}\tau_{e,z}$ which is different for the two layers which can be interpreted as interlayer vortex.

X. APPENDIX C: SPACE-DEPENDENT ORDER PARAMETER

The order parameter presented in the phase diagram of the main text is the sum of local order parameters over the moiré unit cell. Here, we present the order parameter for valley polarization (τ_z) for some parameters, discriminating layer and sublattice.

We can also denote this quantity as additive flux as we use the formula

$$\text{Im } \Delta_{++}(\mathbf{r}_i) = \text{Im} \sum_{n=0,1,2} \rho_{\mathbf{r}_i \pm \delta_n, \mathbf{r}_i \pm \delta_{n+1}}. \quad (92)$$

Alternatively, we can also define a different quantity which we label multiplicative flux as we use the formula

$$\text{Im } \Delta_{++}(\mathbf{r}_i) = \text{Im} \left(\prod_{n=0,1,2} \rho_{\mathbf{r}_i \pm \delta_n, \mathbf{r}_i \pm \delta_{n+1}} \right)^{1/3}. \quad (93)$$

Even though both quantities yield similar order parameters, the spacial distribution is quite different. As the formulas using the sum have a clear interpretation also beyond the intra-sublattice, intravalley channel, we will only discuss the order parameters using this definition.

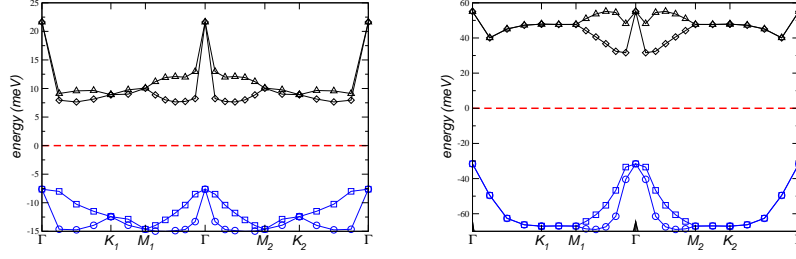


FIG. 17. Hartree Fock bands for $\nu = 0$ and $U = 0.5\text{eV}$ at $\epsilon = 60$ (left) and $\epsilon = 12$ (right). The chemical potential is set to zero and indicated by the red dashed line.

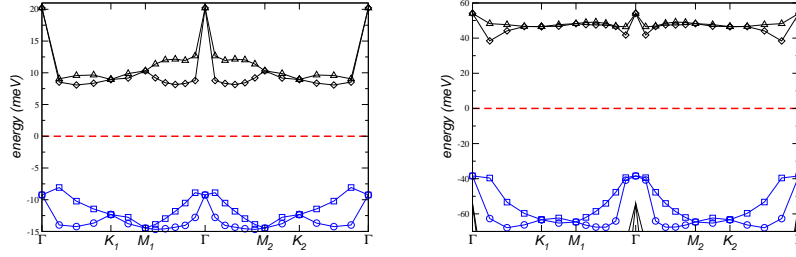


FIG. 18. Hartree Fock bands for $\nu = 0$ and $U = 4.0\text{eV}$ at $\epsilon = 60$ (left) and $\epsilon = 12$ (right). The chemical potential is set to zero and indicated by the red dashed line.

-
- ¹ J. M. B. L. dos Santos, N. M. R. Peres, and A. H. C. Neto, *Physical Review Letters* **99** (2007).
 - ² G. Li, A. Luican, J. M. B. Lopes dos Santos, A. H. Castro Neto, A. Reina, J. Kong, and E. Y. Andrei, *Nature Physics* **6**, 109 (2010).
 - ³ E. Suárez Morell, J. D. Correa, P. Vargas, M. Pacheco, and Z. Barticevic, *Phys. Rev. B* **82**, 121407 (2010).
 - ⁴ R. Bistritzer and A. H. MacDonald, *Proceedings of the National Academy of Sciences* **108**, 12233 (2011).
 - ⁵ Y. Cao, V. Fatemi, A. Demir, S. Fang, S. L. Tomarken, J. Y. Luo, J. D. Sanchez-Yamagishi, K. Watanabe, T. Taniguchi, E. Kaxiras, R. C. Ashoori, and P. Jarillo-Herrero, *Nature* **556**, 80 (2018).
 - ⁶ Y. Cao, V. Fatemi, S. Fang, K. Watanabe, T. Taniguchi, E. Kaxiras, and P. Jarillo-Herrero, *Nature* **556**, 43 (2018).
 - ⁷ P. A. Lee, N. Nagaosa, and X.-G. Wen, *Rev. Mod. Phys.* **78**, 17 (2006).
 - ⁸ A. L. Sharpe, E. J. Fox, A. W. Barnard, J. Finney, K. Watanabe, T. Taniguchi, M. A. Kastner, and D. Goldhaber-Gordon, *Science* **365**, 605 (2019).
 - ⁹ A. L. Sharpe, E. J. Fox, A. W. Barnard, J. Finney, K. Watanabe, T. Taniguchi, M. A. Kastner, and D. Goldhaber-Gordon, *Nano Letters* **21**, 4299 (2021).
 - ¹⁰ P. Moon and M. Koshino, *Phys. Rev. B* **85**, 195458 (2012).
 - ¹¹ H. C. Po, L. Zou, A. Vishwanath, and T. Senthil, *Phys. Rev. X* **8**, 031089 (2018).
 - ¹² P. J. Ledwith, G. Tarnopolsky, E. Khalaf, and A. Vishwanath, *Phys. Rev. Res.* **2**, 023237 (2020).
 - ¹³ Y. Xie, A. T. Pierce, J. M. Park, D. E. Parker, E. Khalaf, P. Ledwith, Y. Cao, S. H. Lee, S. Chen, P. R. Forrester, K. Watanabe, T. Taniguchi, A. Vishwanath, P. Jarillo-Herrero, and A. Yacoby, *Nature* **600**, 439 (2021).
 - ¹⁴ A. T. Pierce, Y. Xie, J. M. Park, E. Khalaf, S. H. Lee, Y. Cao, D. E. Parker, P. R. Forrester, S. Chen, K. Watanabe, T. Taniguchi, A. Vishwanath, P. Jarillo-Herrero, and A. Yacoby, *Nature Physics* **17**, 1210 (2021).
 - ¹⁵ M. Oh, K. P. Nuckolls, D. Wong, R. L. Lee, X. Liu, K. Watanabe, T. Taniguchi, and A. Yazdani, *Nature* **600**, 240 (2021).
 - ¹⁶ B. Roy and V. Juričić, *Phys. Rev. B* **99**, 121407 (2019).
 - ¹⁷ Z. A. H. Goodwin, F. Corsetti, A. A. Mostofi, and J. Lischner, *Phys. Rev. B* **100**, 235424 (2019).
 - ¹⁸ E. Lake, A. S. Patri, and T. Senthil, *Phys. Rev. B* **106**, 104506 (2022).
 - ¹⁹ Y. Cao, D. Chowdhury, D. Rodan-Legrain, O. Rubies-Bigorda, K. Watanabe, T. Taniguchi, T. Senthil, and P. Jarillo-Herrero, *Phys. Rev. Lett.* **124**, 076801 (2020).
 - ²⁰ J. González and T. Stauber, *Phys. Rev. Lett.* **124**, 186801 (2020).
 - ²¹ A. Jaoui, I. Das, G. Di Battista, J. Díez-Mérida, X. Lu, K. Watanabe, T. Taniguchi, H. Ishizuka, L. Levitov, and D. K. Efetov, *Nature Physics* **18**, 633 (2022).
 - ²² T. Stauber and J. González, *Nature Physics* **18**, 619 (2022).
 - ²³ B. Lian, Z. Wang, and B. A. Bernevig, *Physical Review Letters* **122** (2019).
 - ²⁴ F. Wu, A. H. MacDonald, and I. Martin, *Phys. Rev. Lett.*

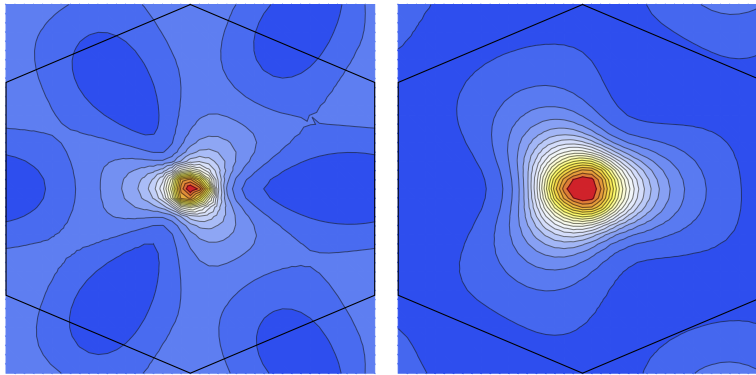


FIG. 19. Energy contour plot of the Hartree Fock band for $\nu = -2$ and $U = 0.5\text{eV}$ at $\epsilon = 60$ (left) and $\epsilon = 12$ (right).

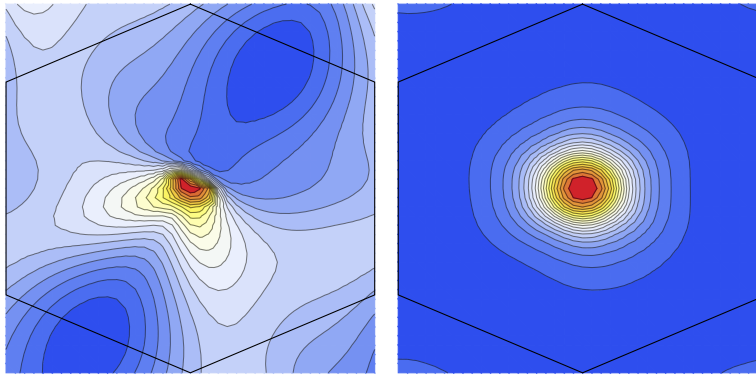


FIG. 20. Energy contour plot of the Hartree Fock band for $\nu = -2$ and $U = 4.0\text{eV}$ at $\epsilon = 60$ (left) and $\epsilon = 12$ (right).

- 121, 257001 (2018).
- ²⁵ J. M. Park, Y. Cao, L.-Q. Xia, S. Sun, K. Watanabe, T. Taniguchi, and P. Jarillo-Herrero, *Nature Materials* **21**, 877 (2022).
- ²⁶ J. M. Park, Y. Cao, K. Watanabe, T. Taniguchi, and P. Jarillo-Herrero, *Nature* **590**, 249 (2021).
- ²⁷ Z. Hao, A. M. Zimmerman, P. Ledwith, E. Khalaf, D. H. Najafabadi, K. Watanabe, T. Taniguchi, A. Vishwanath, and P. Kim, *Science* **371**, 1133 (2021).
- ²⁸ Y. Cao, J. M. Park, K. Watanabe, T. Taniguchi, and P. Jarillo-Herrero, *Nature* **595**, 526 (2021).
- ²⁹ E. Lake and T. Senthil, *Phys. Rev. B* **104**, 174505 (2021).
- ³⁰ M. Christos, S. Sachdev, and M. S. Scheurer, *Phys. Rev. X* **12**, 021018 (2022).
- ³¹ M. Christos, S. Sachdev, and M. S. Scheurer, *Nature Communications* **14**, 7134 (2023).
- ³² J. González and T. Stauber, *Nature Communications* **14**, 2746 (2023).
- ³³ J. Kang and O. Vafek, *Phys. Rev. Lett.* **122**, 246401 (2019).
- ³⁴ K. Seo, V. N. Kotov, and B. Uchoa, *Phys. Rev. Lett.* **122**, 246402 (2019).
- ³⁵ P. Stepanov, I. Das, X. Lu, A. Fahimniya, K. Watanabe, T. Taniguchi, F. H. L. Koppens, J. Lischner, L. Levitov, and D. K. Efetov, *Nature* **583**, 375 (2020).
- ³⁶ N. Bultinck, E. Khalaf, S. Liu, S. Chatterjee, A. Vishwanath, and M. P. Zaletel, *Phys. Rev. X* **10**, 031034 (2020).
- ³⁷ Z.-D. Song, B. Lian, N. Regnault, and B. A. Bernevig, *Phys. Rev. B* **103**, 205412 (2021).
- ³⁸ B. A. Bernevig, Z.-D. Song, N. Regnault, and B. Lian, *Phys. Rev. B* **103**, 205413 (2021).
- ³⁹ B. Lian, Z.-D. Song, N. Regnault, D. K. Efetov, A. Yazdani, and B. A. Bernevig, *Phys. Rev. B* **103**, 205414 (2021).
- ⁴⁰ D. Călugăru, N. Regnault, M. Oh, K. P. Nuckolls, D. Wong, R. L. Lee, A. Yazdani, O. Vafek, and B. A. Bernevig, *Phys. Rev. Lett.* **129**, 117602 (2022).
- ⁴¹ G. Wagner, Y. H. Kwan, N. Bultinck, S. H. Simon, and S. A. Parameswaran, *Phys. Rev. Lett.* **128**, 156401 (2022).
- ⁴² X. Liu, Z. Wang, K. Watanabe, T. Taniguchi, O. Vafek, and J. I. A. Li, *Science* **371**, 1261 (2021), <https://www.science.org/doi/pdf/10.1126/science.abb8754>.
- ⁴³ K. P. Nuckolls, R. L. Lee, M. Oh, D. Wong, T. Soejima, J. P. Hong, D. Călugăru, J. Herzog-Arbeitman, B. A. Bernevig, K. Watanabe, T. Taniguchi, N. Regnault, M. P. Zaletel, and A. Yazdani, *Nature* **620**, 525 (2023).
- ⁴⁴ H. Kim, Y. Choi, É. Lantagne-Hurtubise, C. Lewandowski, A. Thomson, L. Kong, H. Zhou, E. Baum, Y. Zhang, L. Holleis, K. Watanabe, T. Taniguchi, A. F. Young, J. Alicea, and S. Nadj-Perge, *Nature* **623**, 942 (2023).
- ⁴⁵ Y. Cao, D. Rodan-Legrain, J. M. Park, N. F. Q. Yuan, K. Watanabe, T. Taniguchi, R. M. Fernandes, L. Fu, and P. Jarillo-Herrero, *Science* **372**, 264 (2021), <https://www.science.org/doi/pdf/10.1126/science.abc2836>.
- ⁴⁶ S. Carr, S. Fang, P. Jarillo-Herrero, and E. Kaxiras, *Phys.*

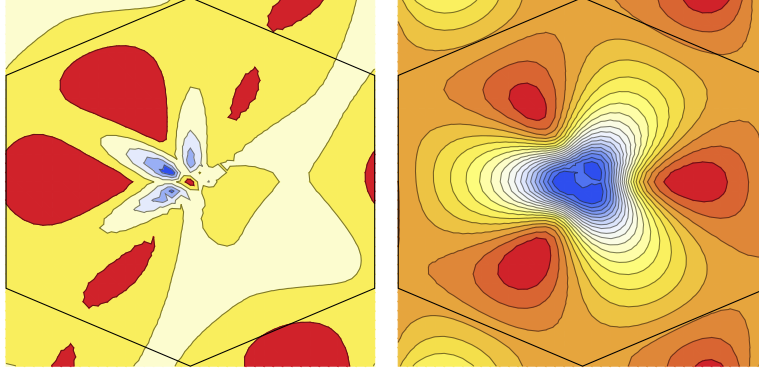


FIG. 21. Energy contour plot of the Hartree Fock band for $\nu = 2$ and $U = 0.5\text{eV}$ at $\epsilon = 60$ (left) and $\epsilon = 12$ (right). The chemical potential is set to zero and indicated by the red dashed line.

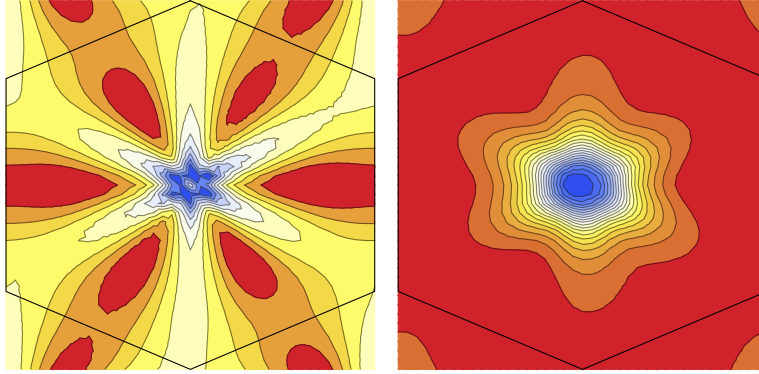


FIG. 22. Energy contour plot of the Hartree Fock band for $\nu = 2$ and $U = 4.0\text{eV}$ at $\epsilon = 60$ (left) and $\epsilon = 12$ (right). The chemical potential is set to zero and indicated by the red dashed line.

- Rev. B **98**, 085144 (2018).
- ⁴⁷ M. Yankowitz, S. Chen, H. Polshyn, Y. Zhang, K. Watanabe, T. Taniguchi, D. Graf, A. F. Young, and C. R. Dean, *Science* **363**, 1059 (2019).
- ⁴⁸ Y. H. Kwan, G. Wagner, N. Bultinck, S. H. Simon, E. Berg, and S. A. Parameswaran, “Electron-phonon coupling and competing kekulé orders in twisted bilayer graphene,” (2023), arXiv:2303.13602 [cond-mat.str-el].
- ⁴⁹ See Supplemental Material for details on the tight-binding approach and Hartree-Fock theory, the algorithm to obtain the reduced density matrix, discussion of the phase diagram as well as additional plots of the band structure.
- ⁵⁰ P. Moon and M. Koshino, *Phys. Rev. B* **87**, 205404 (2013).
- ⁵¹ R. E. Throckmorton and O. Vafek, *Phys. Rev. B* **86**, 115447 (2012).
- ⁵² Y. Saito, J. Ge, K. Watanabe, T. Taniguchi, and A. F. Young, *Nature Physics* **16**, 926 (2020).
- ⁵³ P. Stepanov, I. Das, X. Lu, A. Fahimniya, K. Watanabe, T. Taniguchi, F. H. L. Koppens, J. Lischner, L. Levitov, and D. K. Efetov, *Nature* **583**, 375 (2020).
- ⁵⁴ W. Kohn, *Phys. Rev.* **133**, A171 (1964).
- ⁵⁵ W. Kohn, *Phys. Rev. Lett.* **76**, 3168 (1996).
- ⁵⁶ Z.-D. Song and B. A. Bernevig, *Phys. Rev. Lett.* **129**, 047601 (2022).
- ⁵⁷ M. S. Sánchez and T. Stauber, arXiv:2302.00884.
- ⁵⁸ J. Gonzalez and T. Stauber, *Physical Review B* **104** (2021).
- ⁵⁹ W. Kohn and J. M. Luttinger, *Phys. Rev. Lett.* **15**, 524 (1965).
- ⁶⁰ M. A. Baranov, A. V. Chubukov, and M. Yu. Kagan, *International Journal of Modern Physics B* **06**, 2471 (1992).
- ⁶¹ D. J. Scalapino, E. Loh, and J. E. Hirsch, *Phys. Rev. B* **35**, 6694 (1987).
- ⁶² Y. Zhang, R. Polski, A. Thomson, É. Lantagne-Hurtubise, C. Lewandowski, H. Zhou, K. Watanabe, T. Taniguchi, J. Alicea, and S. Nadj-Perge, *Nature* **613**, 268 (2023).
- ⁶³ L. Holleis, C. L. Patterson, Y. Zhang, H. M. Yoo, H. Zhou, T. Taniguchi, K. Watanabe, S. Nadj-Perge, and A. F. Young, arXiv:2303.00742.

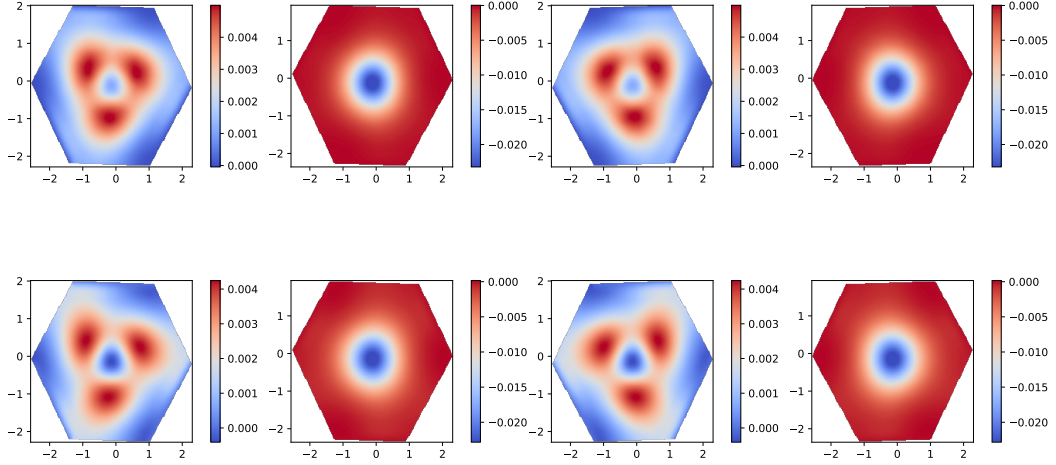


FIG. 23. Additive flux of the Hartree Fock Hamiltonian for the sublattice A and layer 1 (left), B1 (center left), A2 (center right), B2 (right) with $U = 0.5\text{eV}$ for $\nu = -2$ and $\alpha = \frac{e^2}{4\pi\epsilon_0\epsilon} = 0.1\text{eV} \times a$ (left) and $\alpha = \frac{e^2}{4\pi\epsilon_0\epsilon} = 0.5\text{eV} \times a$ (right).

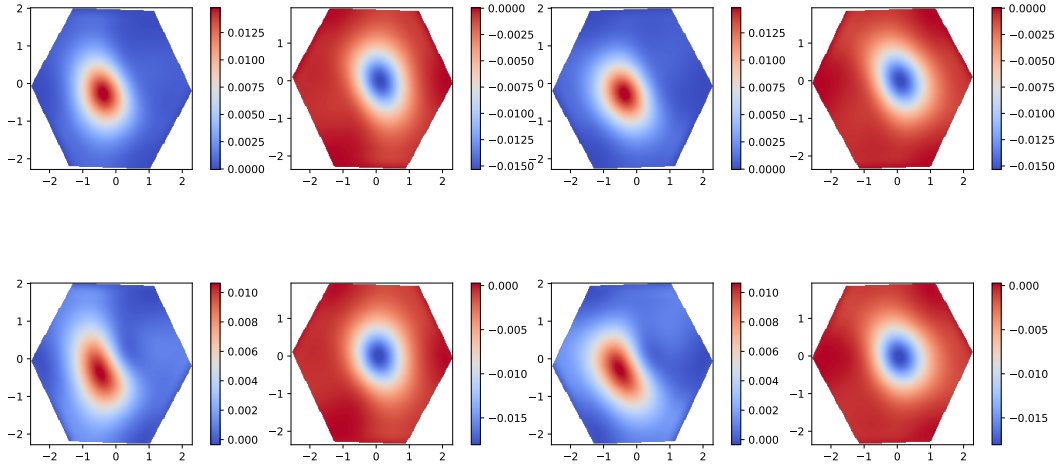


FIG. 24. Additive flux of the Hartree Fock Hamiltonian for the sublattice A and layer 1 (left), B1 (center left), A2 (center right), B2 (right) with $U = 4\text{eV}$ for $n = -2$ and $\alpha = \frac{e^2}{4\pi\epsilon_0\epsilon} = 0.1\text{eV} \times a$ (left) and $\alpha = \frac{e^2}{4\pi\epsilon_0\epsilon} = 0.5\text{eV} \times a$ (right) for the valley polarized phase.

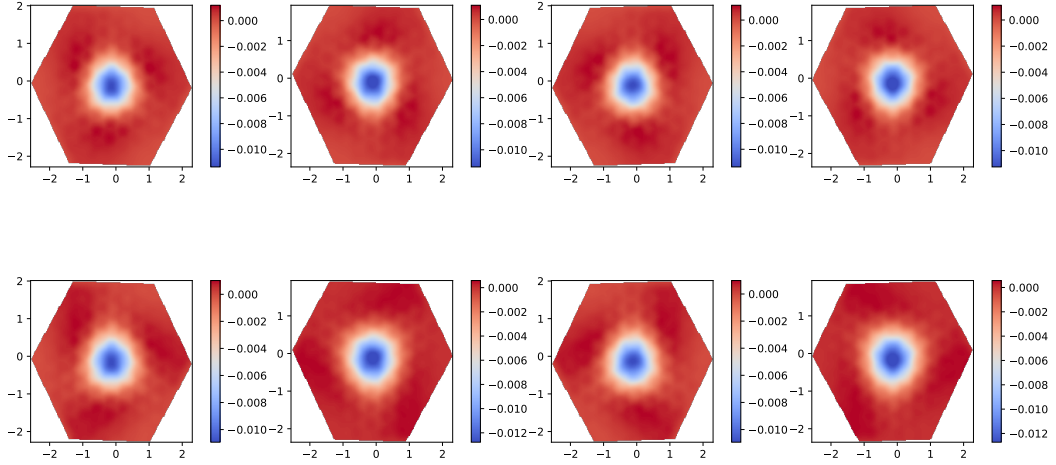


FIG. 25. Additive flux of the Hartree Fock Hamiltonian for the sublattice A and layer 1 (left), B1 (center left), A2 (center right), B2 (right) with $U = 4\text{eV}$ for $n = -2$ and $\alpha = \frac{e^2}{4\pi\epsilon_0\epsilon} = 0.1\text{eV} \times a$ (left) and $\alpha = \frac{e^2}{4\pi\epsilon_0\epsilon} = 0.5\text{eV} \times a$ (right) for the valley coherent phase.

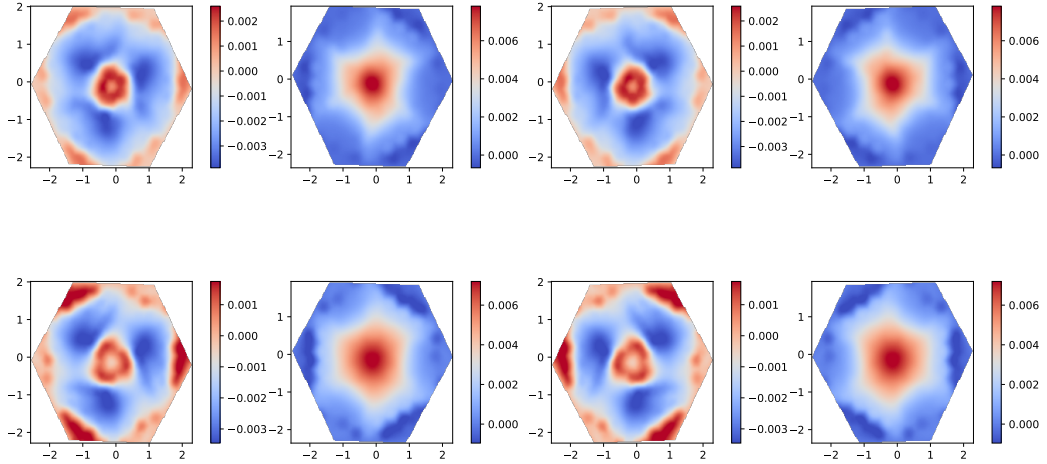


FIG. 26. Multiplicable flux of the Hartree Fock Hamiltonian for the sublattice A and layer 1 (left), B1 (center left), A2 (center right), B2 (right) with $U = 0.5\text{eV}$ for $n = -2$ and $\alpha = \frac{e^2}{4\pi\epsilon_0\epsilon} = 0.1\text{eV} \times a$ (left) and $\alpha = \frac{e^2}{4\pi\epsilon_0\epsilon} = 0.5\text{eV} \times a$ (right).

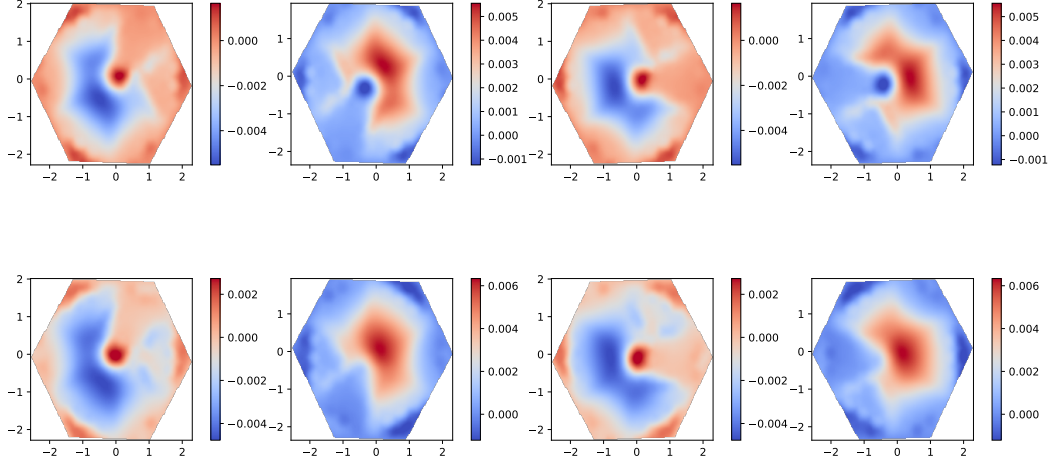


FIG. 27. Multiplicable flux of the Hartree Fock Hamiltonian for the sublattice A and layer 1 (left), B1 (center left), A2 (center right), B2 (right) with $U = 0.5\text{eV}$ for $n = -2$ and $\alpha = \frac{e^2}{4\pi\epsilon_0\epsilon} = 0.1\text{eV} \times a$ (left) and $\alpha = \frac{e^2}{4\pi\epsilon_0\epsilon} = 0.5\text{eV} \times a$ (right) for the valley polarized phase.

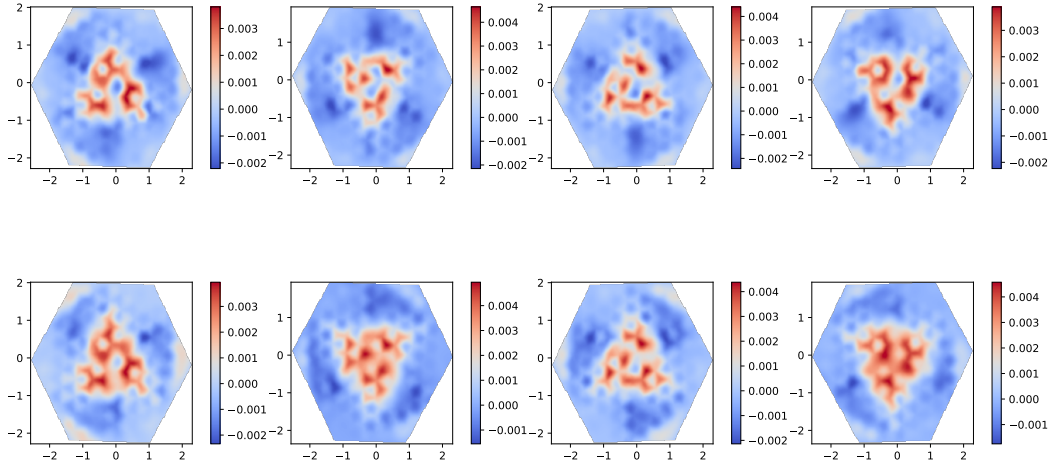


FIG. 28. Multiplicable flux of the Hartree Fock Hamiltonian for the sublattice A and layer 1 (left), B1 (center left), A2 (center right), B2 (right) with $U = 0.5\text{eV}$ for $n = -2$ and $\alpha = \frac{e^2}{4\pi\epsilon_0\epsilon} = 0.1\text{eV} \times a$ (left) and $\alpha = \frac{e^2}{4\pi\epsilon_0\epsilon} = 0.5\text{eV} \times a$ (right) for the valley coherent phase.